

© 2015

YUXIAO ZHOU

ALL RIGHTS RESERVED

**COLLIMATED SOLAR ENERGY ALLOCATION IN
SMART WINDOW
USING MONTE CARLO RAY-TRACING METHOD**

By

YUXIAO ZHOU

A thesis submitted to the

Graduate School-New Brunswick

Rutgers, The State University of New Jersey

In partial fulfillment of the requirements

For the degree of

Master of Science

Graduate Program in Mechanical and Aerospace Engineering

Written under the direction of

Zhixiong Guo

And approved by

New Brunswick, New Jersey

October, 2015

ABSTRACT OF THE THESIS

COLLIMATED SOLAR ENERGY ALLOCATION IN SMART WINDOW
USING MONTE CARLO RAY-TRACING METHOD

By YUXIAO ZHOU

Thesis Director:

Zhixiong Guo

A solar radiative heat transfer model has been developed to study the collimated solar energy harvest in a smart window consisting of multiple silica glass louvers filled with water. The domain is divided into triangular grids, and Monte Carlo method and ray-tracing method are used to allocate energy harvest into grids. The full solar spectrum is divided into discrete bands, and the solar irradiation intensity on each band is distributed among a huge number of independent energy bundles. Band-averaged spectral properties of medium (silica glass and water) are used on each band. Results of different band division methods and different energy bundle numbers are compared to find optimal fits that are both time-saving and accurate. The influence of solar irradiation incoming direction on energy harvest is also discussed.

Keywords: solar radiative heat transfer model, collimated energy harvest, Monte Carlo ray-tracing, band-averaged spectral properties

Nomenclature

AM	air mass
AM	direction cosine of energy packet path along x axis
AL	direction cosine of energy packet path along y axis
β	extinction coefficient (m^{-1})
δ	thickness of silica glass (inch)
DXG	width of an element (inch)
DYG	height of an element (inch)
E_{on}	extraterrestrial irradiation (W/m^2)
$E_{on\lambda}$	spectral extraterrestrial irradiance (W/m^2)
E_{sc}	extraterrestrial solar constant (W/m^2)
E_{sun}	power density at the sun's surface (W/m^2)
\hbar	universal Planck constant ($= 6.626 \times 10^{-34} J \cdot s$)

I	radiative intensity ($\text{W/s} \cdot \text{m}^2 \cdot \text{sr}$) (area normal to rays)
$IDIM, JDIM$	number of nodes on horizontal and vertical edges of the mesh
I_λ	spectral radiative intensity ($\text{W/s} \cdot \text{m}^2 \cdot \text{sr} \cdot \mu\text{m}$) (area normal to rays)
INDGWC	index of next element
IW	index of element boundary
IXT	number of target element in X direction
IYT	number of target element in Y direction
k	universal Boltzmann constant ($= 1.3806488 \times 10^{-23} \text{J/K}$)
k_λ	absorption index
κ	absorption coefficient (m^{-1})
\overline{K}_T	clearness index
NDISP	index of edge property
ρ	density (kg/m^3)
R_{sun}	radius of the sun (m)
R	distance from the sun (m)
R_ϕ	random number defining azimuthal angle of redirection
R_ρ	random number used to determine between reflection and refraction

R_θ	random number defining polar angle of redirection
R_x	random number defining location of ejection
S	traveling length of energy particle
σ	scattering coefficient (m^{-1})
XI, XE	x coordinate where energy packet hits wall
YI, YE	y coordinate where energy packet hits wall

Index

Abstract	ii
Nomenclature	iii
Chapter 1 Introduction	1
1.1 Solar Energy and Solar System	1
1.2 Radiation Properties	3
1.3 Energy Equation and Radiative Transfer Equation	5
1.4 Assumptions and polarization consideration	7
1.5 Smart Window	8
1.6 Physical Model of a Louver	10
1.7 Research Motivation and Outline	11
Chapter 2 Monte Carlo Method	15
2.1 Development and Superiority of Monte Carlo Method	15
2.2 The Random Walk Theory and Random Numbers	17
2.3 Simulation of Redirection	18
2.4 Mesh Generation	25
2.5 Labeling Elements	27

2.6	Program Flow Chart	30
Chapter 3 Solar Irradiation Data		31
3.1	The Solar Constant	31
3.2	Air Mass (AM):	33
3.3	Atmospheric extinction of Solar Radiation	34
3.4	Global Horizontal Irradiation (GHI)	47
3.5	Silica Glass Properties	50
3.6	Water Properties	53
3.7	Weighted Spectral Properties	54
Chapter 4 Influence of Spectral Bands		57
4.1	Choice of Photon Number	57
4.2	Spectral Band Number Division	61
Chapter 5 Influence of Incident Direction		71
5.1	Choice of Spectral Band Number	71
5.2	Angular Variation Analysis	74
5.3	Contour of Louver	76
Chapter 6 Conclusion		80
Reference		83

Chapter 1

Introduction

1.1 Solar Energy and Solar System

The gigantic amount of solar energy falling onto the earth is amazing: 3×10^{24} joules per year [1], most of which remains unutilized while we keep depleting traditional fossil fuels. Distributed Energy Resources (DER) are growing rapidly due to lower cost [2] and acceptable efficiency [3] of their application in small scale power generation facilities that are ready to be integrated into Microgrids (MG). In order to make the integrated system stable, a precise prediction of solar energy harvest behavior in a unit MG is crucial [4].

The *extraterrestrial solar constant* E_{sc} (W/m^2) is defined as the amount of energy from the sun, per unit time, received on a unit area of surface perpendicular to the direction of propagation of the solar radiation, at the earth's mean distance from the sun, outside of the atmosphere [5]. Relationship between intensity of solar irradiation and extraterrestrial solar constant on a planet can be defined by the *inverse-square law* (1-1):

$$E_{sc} = \frac{R_{sun}^2}{R^2} E_{sun} \quad (1-1)$$

where E_{sun} is the intensity at the sun's surface (W/m^2), R_{sun} is the radius of the sun in meters and R is the distance between sun and any planet in solar system. A brief illustration of the planets in solar system is shown in Fig 1.1.

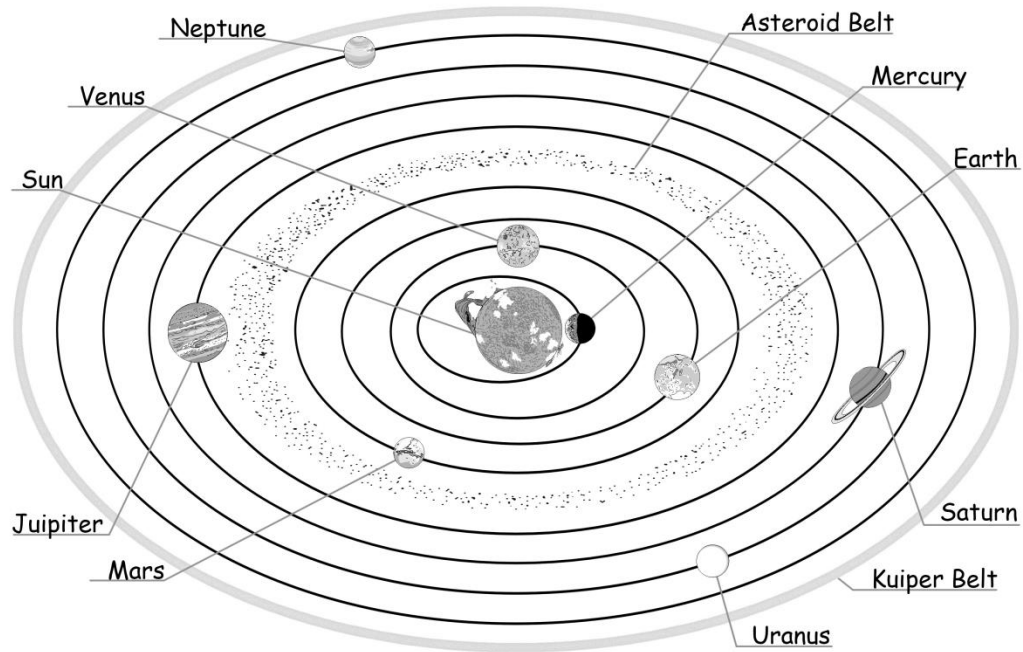


Fig 1.1 The solar system [6]

Table 1.1 below gives standardized mean solar constant at each of the planets in solar system.

Table1.1 mean solar constants at the planets [7]

Planet	Distance $R (\times 10^9 m)$	Mean Solar Constant $E_{sc} (W/m^2)$
Mercury	57	9116.4
Venus	108	2611.0
Earth	150	1366.1
Mars	227	588.6
Jupiter	778	50.5
Saturn	1426	15.04
Uranus	2868	3.72
Neptune	4497	1.51
Pluto	5806	0.878

1.2 Radiation Properties

Electromagnetic waves travels in discrete packets called *quanta*. Instead of thinking about an oscillator of classical frequency ν , we use the fictitious particles, quanta [8], each endowed with energy $\hbar\nu$, where \hbar is the universal Planck constant equal to $6.626 \times 10^{-34} \text{ J} \cdot \text{s}$ [9], as the basic unit, to describe the transmittance of electromagnetic waves. Then the total propagating energy carried by electromagnetic waves can be expressed as

$$E = N \cdot \hbar\nu \quad (1-2)$$

where N is the total number of quantum.

1.2.1 Planck's law:

The blackbody formulation derived by Max Planck shows the spectral distribution of blackbody emissive power, $E_{b\lambda}$, by means of quantum theory. Planck's law is expressed as:

$$E_{b\lambda} = \frac{2\pi\hbar c^2}{\lambda^5 [\exp(\hbar c / \lambda k T) - 1]}, \quad (1-3)$$

where c is the speed of light in vacuum, T is the temperature of blackbody in Kelvin, and k is the universal Boltzmann constant, which equals to $1.3806488 \times 10^{-23}$ J/K.

1.2.2 Radiation Intensity:

The *radiation intensity* is defined as radiative energy flow per unit solid angle and unit area normal to the rays [10]. Solar radiation intensity is strongly wavelength-dependent and non-homogenous in most cases, and spectral intensity and total intensity can be related through integration:

$$I(\mathbf{r}, \vec{s}) = \int_0^\infty I_\lambda(\mathbf{r}, \vec{s}, \lambda) d\lambda \quad (1-4)$$

where \mathbf{r} represents position vector, \vec{s} represents direction vector, and λ represents wavelength ranging from 0 to infinity.

1.2.3 Extinction Coefficient, Absorption Coefficient, Scattering Coefficient and Beer's law:

The *spectral extinction coefficient* β_λ is defined as the fraction of the energy incident on a body that is being absorbed by the body [11]. Then extinction of intensity can be defined as:

$$dI_\lambda = -\beta_\lambda I_\lambda dS, \quad (1-5)$$

where

$$\beta_\lambda = \kappa_\lambda + \sigma_{s,\lambda}. \quad (1-6)$$

κ_λ and $\sigma_{s,\lambda}$ in equation (1-6) stands for *spectral absorption coefficient* and *spectral scattering coefficient*, respectively. Both κ_λ and $\sigma_{s,\lambda}$ have units of reciprocal length.

I_λ is spectral radiation intensity, and dS is a very small path length along propagation direction of radiation. Absorption coefficient and scattering coefficient are usually wavelength-dependent. If we ignore scattering in the process being studied for simplification, absorption is the only way of energy loss as light passes through uniform medium. Integration of the above equation leads to *Beer's law*:

$$I_\lambda = I_{0\lambda} e^{-\kappa_\lambda S}, \quad (1-7)$$

where $I_{0\lambda}$ is the initial spectral radiation intensity of light, and the units of absorption coefficient κ_λ and propagation depth S are inverse meter and meter, respectively.

1.3 Energy Equation and Radiative Transfer Equation

The conventional energy equation can be obtained by studying the energy balance of a control volume. For a control volume of finite size, the first law of thermodynamics requires a balance of conduction, convection, thermal radiation, internal heat sources

such as electrical dissipation, combustion, compression work, viscous dissipation, and energy storage, as shown in Fig 1.2 below [12].

The first law of thermodynamics is then written as

$$\rho c_p \frac{DT}{Dt} = \beta T \frac{DP}{Dt} + \nabla \cdot (k \nabla T - \mathbf{q}_r) + \dot{q} + \Phi \quad (1-8)$$

where ρ is density of control volume, c_p is heat capacity, T is temperature, P stands for pressure, β is coefficient of thermal expansion defined by $\beta = -\frac{1}{\rho} \left(\frac{\partial \rho}{\partial T} \right)_P$, and k is heat conductivity. $\nabla \cdot (k \nabla T)$ is the net contribution of heat conduction to the control volume, \mathbf{q}_r is the radiant flux vector, acting as the contribution of thermal radiation, \dot{q} is the local energy source per unit volume and time, and Φ is the energy generated from viscous dissipation.

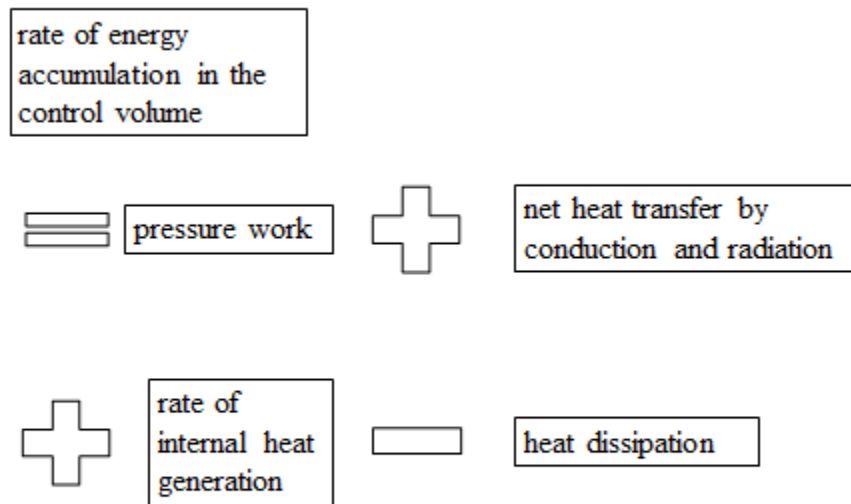


Fig 1.2 Energy balance of a control volume

The *Radiative Transfer Equation* (RTE), which is derived from conservation of radiative energy along path way, is a fundamental equation in radiative heat transfer. By investigating radiative energy flux within a small volume element, over a small path length dS along S , within a small solid angle $d\Omega$ around the direction (θ, ϕ) , and within a small wavelength interval $d\lambda$ around a given wavelength, the steady-state RTE equation can be expressed as (Howell and Siegel, 1992):

$$\frac{\partial I_\lambda(S, \Omega)}{\partial S} = \kappa_\lambda I_{\lambda b}(S) - (\kappa_\lambda + \sigma_{s, \lambda}) I_\lambda(S, \Omega) - \frac{\sigma_{s, \lambda}}{4\pi} \int_{\Omega_i=4\pi} I_\lambda(S, \Omega_i) \Phi_\lambda(\Omega_i, \Omega) d\Omega_i \quad (1-9)$$

where κ_λ is spectral absorption coefficient, $\sigma_{s, \lambda}$ is spectral scattering coefficient, and Φ_λ is phase function.

1.4 Assumptions and polarization consideration

Non-scattering. $\sigma_{s, \lambda} = 0$, thus the integral term is removed from the energy equation which greatly simplifies the RTE to a differential equation.

Isotropic absorption coefficient. $\kappa = f(\lambda)$, which means the value of κ only depends on wavelength of light.

No end effect. We assume the model is infinitely long in z direction. While path length is calculated in 3D, energy allocation is accomplished by projecting the 3D path length onto 2D grid on x - y plane.

Unpolarized light source. Natural light sources emit unpolarized light. For unpolarized solar irradiation, the electric field has no definite orientation regarding the incident plane, thus has equal parallel and perpendicular components. This consideration is reflected in the equation for reflectivity on interface that follows.

1.5 Smart Window

The model used in this thesis is a *smart window* proposed by Dr. N. Madamopoulos at CCNY (private communications). A smart window is a device consists of a series of transparent louvers that can be installed on one side of a window to change penetration depth of sunlight in order to provide deeper lighting into the room, as well as to absorb the infrared part in solar radiation to heat the working fluid inside the louvers. A detailed illustration of a louver is given in Fig. 1.3. Fig. 1.4 shows how louvers are aligned along a window to fulfill all the functions.

Future study of this model will involve mixing particles into the working liquid and maximize absorption through scattering. It can also be designed to truncate sunlight at certain bands for special purposes. For example, in summer, we want to intercept the infrared part to reduce room temperature. To be more complete, the Radiative Transfer Equation (RTE) should be combined with natural convection of liquid inside the tube and conductive heat transfer within the tube wall, while the current radiation-only results are turned into heat flux, and are used as part of the initial conditions in future calculation.

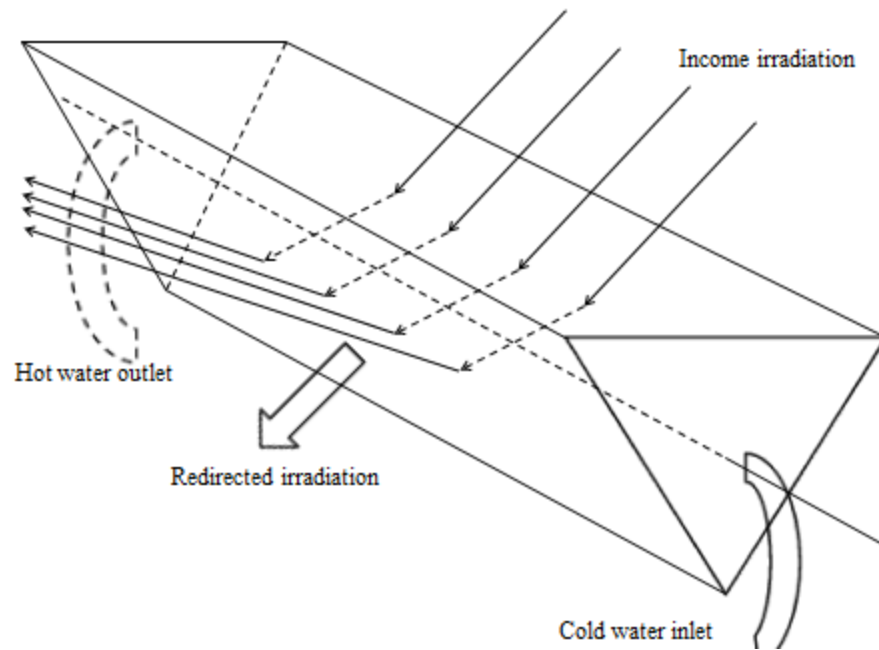


Fig1.3 Brief plot of a louver (from N. Madamopoulos)

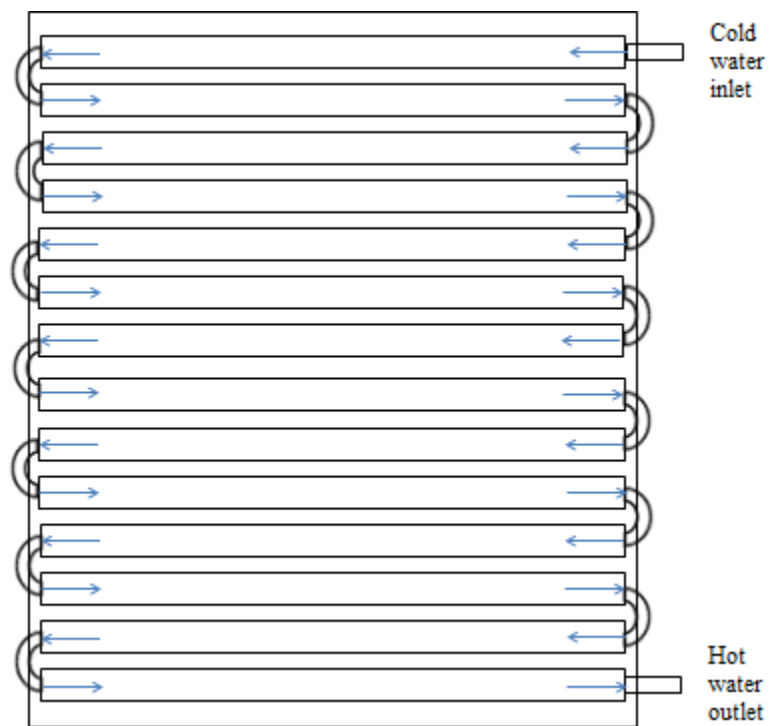


Fig 1.4 Louvers installed inside a window (from N. Madamopoulos)

1.6 Physical Model of a Louver

The physical model being studied in this thesis is a long silica glass louver filled with working liquid (we use pure water as working liquid in this thesis), as shown in Fig 1.5 below.

The cross section of the prismatic louver is an equilateral triangle, which is an assemble of three pieces of uniform silica glass, each with thickness of 0.125 inch, width of 3 inches and length of 33 inches. A brief illustration of the cross section is given in Fig 1.6. Two pieces of plexiglass panels at two ends are used to seal the louver while two brass tubes act as the inlet and outlet of working fluid. Since the louver is very long, for most of the part of the louver, we can ignore end effect.

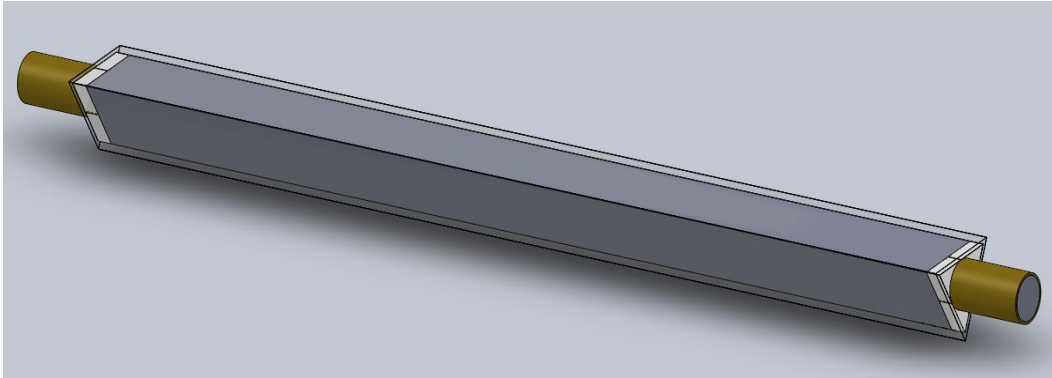


Fig1.5 Physical model of louver

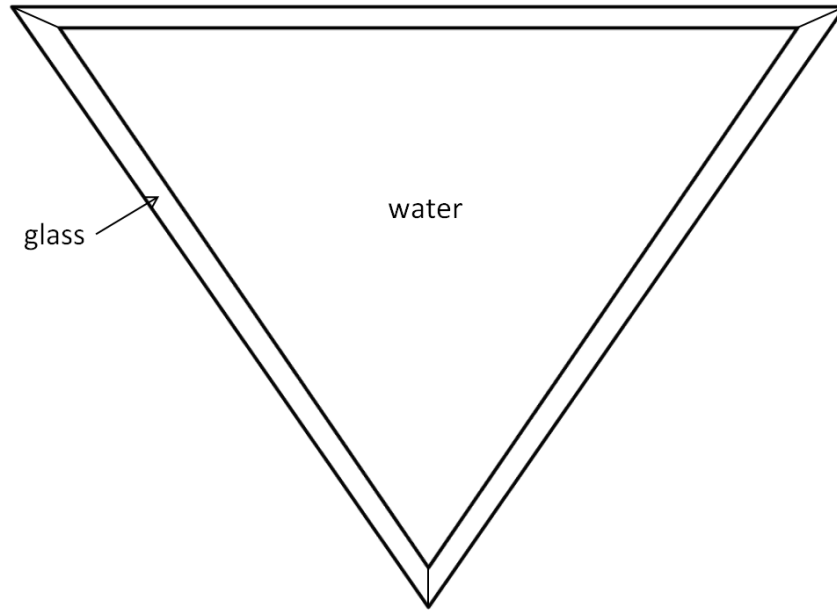


Fig1.6 Cross section of the louver

1.7 Research Motivation and Outline

According to data from EIA (Energy Information Administration), more than half total energy consumption in commercial buildings are spent on lighting and heating yearly as shown in Fig 1.7. Solar energy can provide both lighting and heating, thus utilizing solar energy will save much non-renewable energy consumption.

Currently, most green facilities utilizing solar energy only performs single task, either solar heating or solar photovoltaic power generation, making use of only a certain band of the solar irradiation. Most often seen examples are solar water heater and solar photovoltaic system. A solar water heater is usually installed at rooftop to collect the most solar energy directly and without taking up indoor space. Fig 1.8 gives a brief

illustration of a passive solar water heater. This is a quite traditional field, and design and performance of solar water heater can be found in ref. [5].

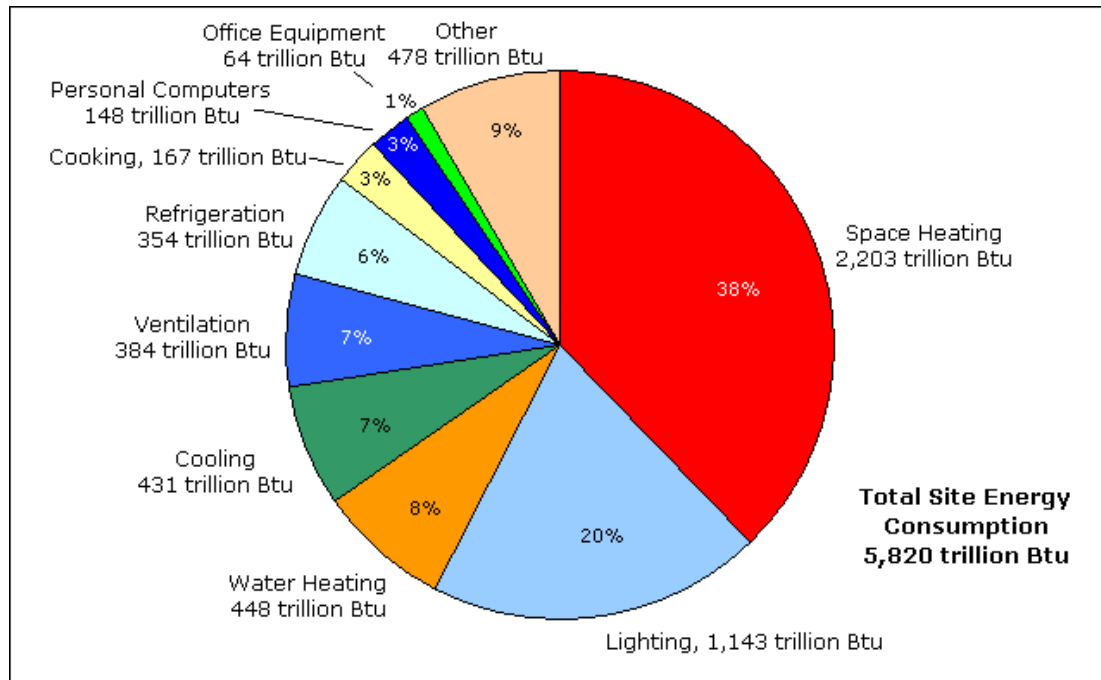


Fig 1.7 Total energy consumption in commercial buildings [13]

A solar photovoltaic system is used to convert sunlight directly to electricity through solar cells (or photovoltaic cells) by the photovoltaic effect. The most effort is put into enhancing solar cell efficiency and minimizing installation costs at the same time to make it more economically efficient. The yearly installation capacity of solar photovoltaic facilities has seen a continuous significant increase worldwide these years [14]. At present, the best reported solar cell is a multi-junction cell having a record of 44.4% efficiency at direct irradiance concentration of $3.02 \times 10^5 \text{ W/m}^2$ [15]. Fig 1.9(a) shows the solar photovoltaic facility installed on a building in Finland and Fig 1.9(b) shows a solar park in England.

A PV/thermal solar hybrid system is a combination of photothermal and photovoltaic processes, utilizes the full solar spectrum efficiently, and is becoming a promising field in green energy facilities. Beam splitting method makes the simulation results of photothermal and photovoltaic (PV) processes more reliable since most of the medium or surface materials used in a solar energy harvest system have highly wavelength-dependent properties.

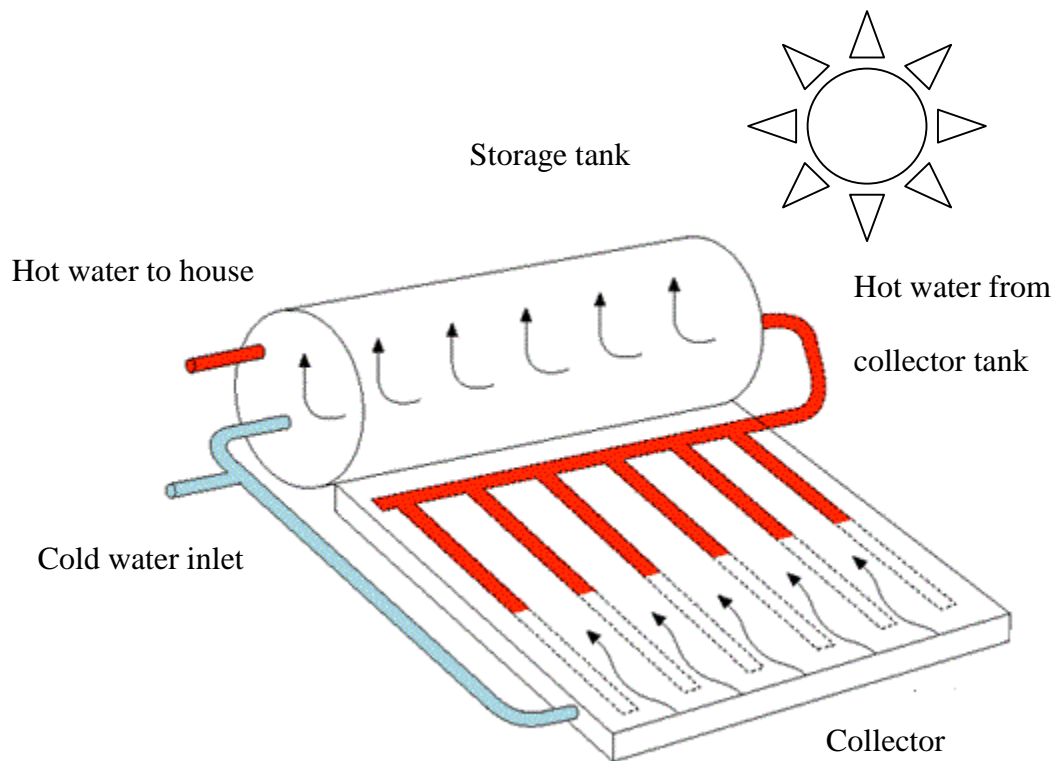


Fig 1.8 A solar water heater [16]



(a)



(b)

Fig1.9 Solar photovoltaic systems

((a): building-integrated solar panels in Helsinki, Finland [17]; (b): Westmill solar park in South East England [18])

This chapter is a brief introduction to solar energy, research background and motivation. Chapter 2 mainly discusses the statistical Monte Carlo method, mesh generation, and program flow chart. Chapter 3 provides all the data used in the program, such as solar spectral intensity, silica glass and water properties, and most important, atmospheric attenuation considerations. Chapter 4 concentrates on influence of photon on the simulation results. Results of different photon numbers are compared to get an accurate and computationally effective photon number choice. In the last section of this chapter, ways of dividing the full spectrum into 3, 10, 20 and 40 bands are listed. Chapter 5 discusses the influence of spectral band number and incident direction on energy harvest. Energy distribution of different incident directions is compared to illustrate angular influence and the importance of angular adjustment during solar energy collection process. Chapter 6 is the conclusion.

Chapter 2

Monte Carlo Method

2.1 Development and Superiority of Monte Carlo Method

Monte Carlo method is used to create simulated observations of physical processes based on statistical characteristics and was associated with formal techniques in the 1940's [19]. The method was at first developed to give numerical estimates of nuclear weapon behaviors during World War II, when experiments were not sufficient to provide accurate predictions. Howell was among the first to introduce Monte Carlo method into radiative heat transfer [20].

The complexity of radiative heat transfer problem lies in the nature of the differential-integral property of RTE. Besides, the spectral and directional dependence of surface and participating medium properties, as well as the existence of anisotropic scattering further add difficulty to the solvability of RTE. The common numerical techniques for solving the radiative heat transfer problem largely rely on various degrees of approximation [21].

The major tribute of Monte Carlo method in radiative heat transfer is that it provides a solution without making approximations, and the accuracy mainly depends on sampling size. The development of high-speed digital computer has made Monte Carlo an acceptable method in solving problems where closed-form solutions cannot be achieved easily using finite difference and finite element methods, such as radiation problems in complicated geometry with anisotropic medium properties. Fig 2.1 schematically shows the superiority of Monte Carlo method as the complexity of problem increases. We can see that the solution effort of conventional methods increases rapidly as the problem becomes complicated, and that beyond a certain critical complexity, Monte Carlo method becomes more preferable. Like other statistical methods, Monte Carlo method is also subject to some unavoidable statistical error of order $O(\frac{1}{\sqrt{N}})$, where N is the size of chosen sample [22].

Simulation of radiative energy redistribution in a system is achieved by tracing a large number of energy bundles (photons) from the point of emission till the point of extinction. A large number of energy bundles come into the system from any point on certain exterior surfaces (we take the surface facing the sun as the surface where irradiation entering through in this thesis). The ejection location and redirection of energy packets are all decided by Monte Carlo method.

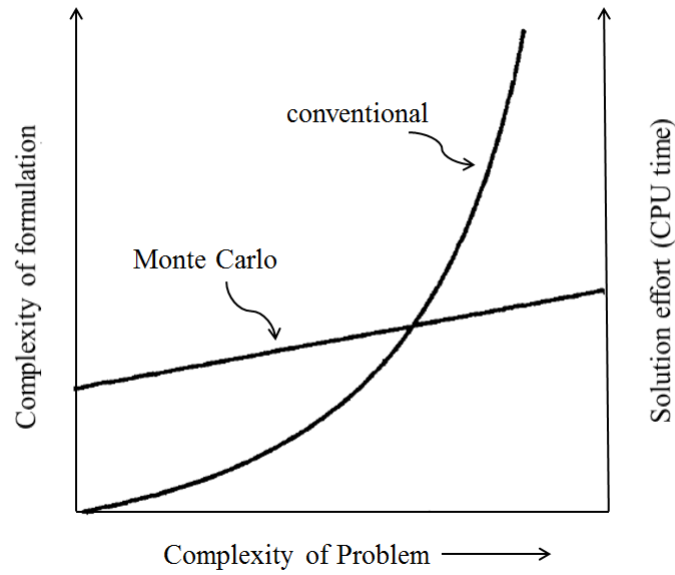


Fig 2.1 Comparison of Monte Carlo and conventional solution techniques [10]

2.2 The Random Walk Theory and Random Numbers

The first definition of *random walk* was brought up by Karl Pearson in 1905, to describe a planar sequence of n steps each uninfluenced by prior steps, and each with identical fixed length into uniformly random directions [23]. It was first introduced to study the infiltration rate of a given species into possible habitats [24], and now it plays key role in areas such as distributed computing and communication networks. In thermal radiation model, random walk theory is used to trace energy packets with the understanding that each diffuse reflection process at an interface is independent of income direction.

A *random number* is a number chosen without sequence from a large set of numbers spaced at equivalued intervals [11]. In most cases, instead of real random numbers, *pseudorandom numbers* are generated within computers using *pseudorandom number*

generators (PNG). The advantage of using a PNG is that every calculation can be repeated as many times as needed, even though periodicity appears near one billion generated numbers, together with linear and nonlinear correlations [25]. The random number R generated in our FORTRAN program is a real number varying between 0 and 1, with different subscripts in different random processes.

2.3 Simulation of Redirection

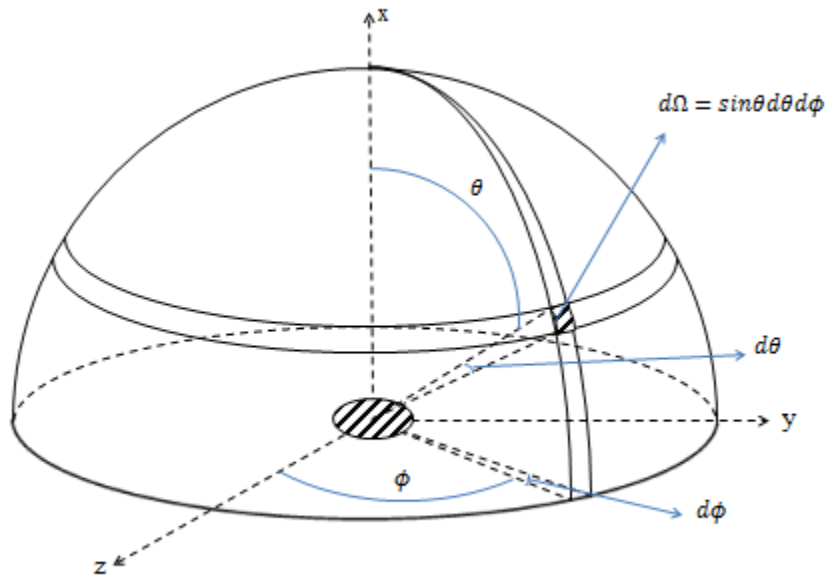


Fig 2.2 Angles of radiative energy emitted from a wall element

Each energy bundle (or photon) is non-dispensable during the ray tracing process and can only travel in one direction at interface instead of possibly being split in real cases.

Energy bundles enter the system at random location, but the number of photons entering the system through each grid is uniform. The incoming location within each grid is decided by a random number. A new direction has to be decided each time an energy

bundle hits an interface. The redirection of diffuse reflection is completely decided by Monte Carlo method within the azimuthal $[0, 2\pi]$ space and polar $[0, \frac{\pi}{2}]$ space.

2.3.1 Azimuthal direction:

Since energy bundles are redirected uniformly within the $(0 - 2\pi)$ space in ϕ direction, the azimuthal random number can be directly determined from:

$$R_\phi = \frac{\phi}{2\pi} \quad (2-1)$$

where R_ϕ is the random number. Thus,

$$\phi = 2\pi R_\phi. \quad (2-2)$$

2.3.2 Polar direction:

Random number R_θ stands for the possibility of energy bundle emitted from a wall element that fall within polar angle $(0, \theta)$. It is defined as:

$$R_\theta = \frac{\text{energy fall within polar angle } (0, \theta)}{\text{total energy emitted into hemisphere}}$$

$$= \frac{\int_0^{2\pi} d\phi \cdot I \cdot \int_0^\theta \cos\theta \cdot \sin\theta d\theta}{\pi \cdot I}$$

$$= \int_0^\theta 2 \cdot \cos\theta \cdot \sin\theta d\theta$$

$$R_\theta = 1 - \cos^2\theta. \quad (2-3)$$

Thus,

$$\theta = \cos^{-1} \sqrt{1 - R_\theta}. \quad (2-4)$$

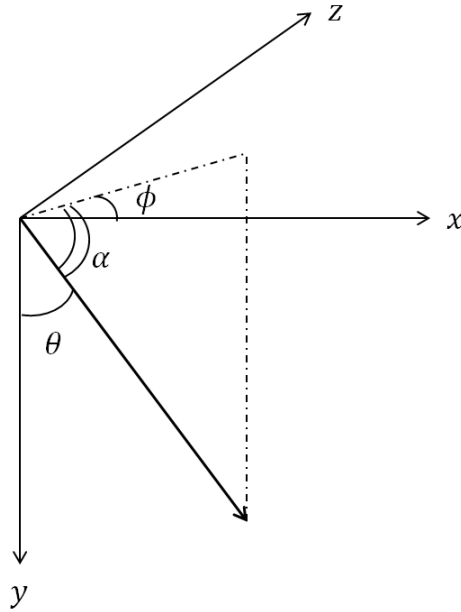


Fig 2.3 Angles of radiative energy emission

2.3.3 Simulation of ejection location:

The ejection location of photon on a grid is decided by

$$X_0 = IXT + R_x, \quad (2-5)$$

where IXT is the grid number of emission grid, and R_x is the corresponding random number.

2.3.4 Simulation of reflection and refraction:

The relationship between the directions of incoming and refracted rays is defined by

Snell's law:

$$n_i \sin \theta_i = n_r \sin \theta_r, \quad (2-6)$$

where n_i and n_r are refractive indices of medium on two sides of the interface, θ_i and θ_r represent the *angle of incidence* and *angle of refraction*, respectively.

If $n_i > n_r$, according to Snell's law, $\theta_i < \theta_r$ is always true. So there exists a critical angle, when angle of incidence $\theta_i > \theta_c$, θ_r becomes greater than $\frac{\pi}{2}$, and the incident radiation is entirely reflected back into the incoming medium. The equation for critical angle is given by:

$$\theta_c = \sin^{-1} \left(\frac{n_r}{n_i} \right). \quad (2-7)$$

The plane of incidence is the plane containing both normal to the interface and the incident direction. If amplitude of a wave is in the plane of incidence, we say the wave is parallel to the plane of incidence. Similarly, we can also define wave that is perpendicular to the plane of incidence. An arbitrary wave can be decomposed into parallel and perpendicular components due to the vector properties of electromagnetic wave. Since we consider unpolarized incident radiation, the comprehensive reflectivity should have equal weight of parallel and perpendicular components. The reflectivity of incident radiation on interface is given by Fresnel equation (Modest, 1993):

$$\rho = \frac{1}{2} \left[\frac{\tan^2(\theta_i - \theta_r)}{\tan^2(\theta_i + \theta_r)} + \frac{\sin^2(\theta_i - \theta_r)}{\sin^2(\theta_i + \theta_r)} \right], \quad (2-8)$$

where the first term in the bracket represents parallel part ρ_{\parallel} and the second term in the bracket represents perpendicular part ρ_{\perp} of the unpolarized incident radiation.

A random number R_ρ is generated and compared with the reflectivity in order to decide the new direction of random walk. A brief process of this process is given in Fig 2.4 below.

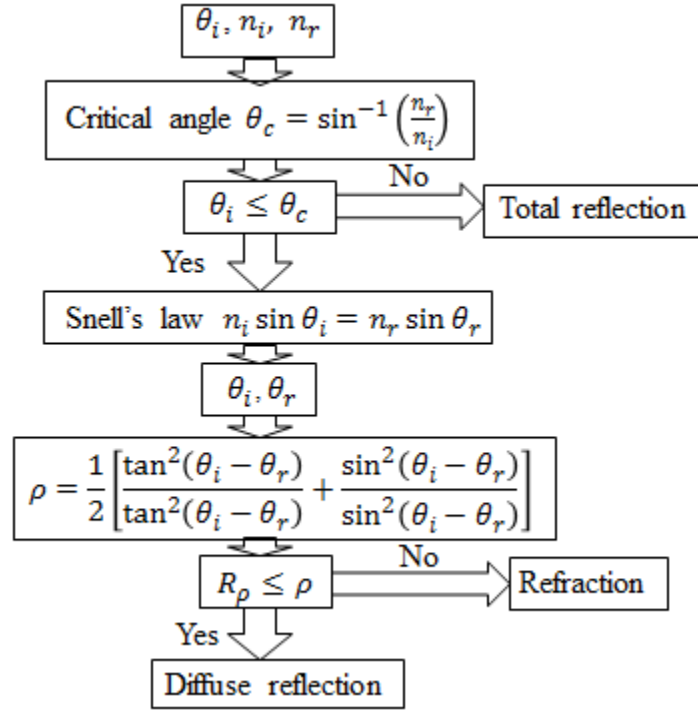


Fig 2.4 Flow chart of redirection determination

2.3.5 Simulation of extinction:

To determine whether a traced energy bundle is absorbed, the current radiative intensity I is compared with a certain criterion I_{bound} , which is a pre-set value representing 0.01% of initial intensity. Once $I < I_{bound}$, current energy bundle is treated as completely absorbed, and all remaining energy of this bundle is added to current grid.

2.3.6 3D path length consideration:

The model is infinite long in z direction. In the process of allocating emission and reflection coordinates, we convert the real condition to a 2D case by projecting the real path length onto front surface (current surface). This process doesn't affect the accuracy since while we account energy absorption on other parallel surfaces onto current surface, our current surface also stands in way of photon path of other surfaces. The existence of the second process makes 2D energy allocation applicable. All surfaces are in fact interchangeable, thus we can take any surface as current surface along z direction. But we still need to consider path length in 3D since the real absorption process takes place along 3D path length instead of 2D path length. The 3D path length is labeled as $SMIN$ in Fig 2.5 below. And the energy allocation is decided by the starting and end points projected onto x - y plane.

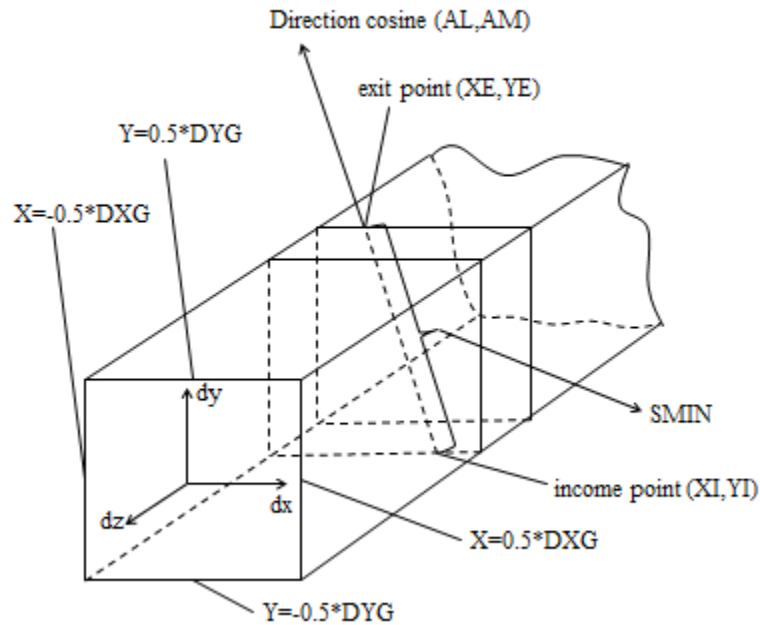


Fig 2.5 3D path length consideration [26]

2.3.7 Direction Transformation in 3D:

The *Transformation Matrix* between two different coordinates can transform vector in one coordinate to the other. In our calculation, the (θ, ϕ) generated through Monte Carlo method is the relative direction to the surface of emission, however, after the energy bundle is redirected, we need to calculate the real direction of the energy bundle in the whole louver system in order to fulfill ray tracing. Still, when the energy bundle arrives at a new destination surface, a new set of (θ, ϕ) needs to be recalculated since redirection of energy bundle will need income angle relative to the new surface to decide between refraction and reflection. According to ref. [27], for two different orthogonal, right-hand sided coordinate systems A and A' , the unit vectors of which are $\mathbf{i}_1, \mathbf{i}_2, \mathbf{i}_3$ and $\mathbf{i}'_1, \mathbf{i}'_2, \mathbf{i}'_3$ respectively, as shown in Fig 2.6 on next page. The transformation matrix T that fulfills $A' = T \cdot A$ is defined as:

$$T = \begin{pmatrix} \mathbf{i}'_1 \cdot \mathbf{i}_1 & \mathbf{i}'_1 \cdot \mathbf{i}_2 & \mathbf{i}'_1 \cdot \mathbf{i}_3 \\ \mathbf{i}'_2 \cdot \mathbf{i}_1 & \mathbf{i}'_2 \cdot \mathbf{i}_2 & \mathbf{i}'_2 \cdot \mathbf{i}_3 \\ \mathbf{i}'_3 \cdot \mathbf{i}_1 & \mathbf{i}'_3 \cdot \mathbf{i}_2 & \mathbf{i}'_3 \cdot \mathbf{i}_3 \end{pmatrix}. \quad (2-9)$$

In the louver model, we have 6 surfaces in all, and the unit vector of top surface is defined as the reference coordinate. Each time an energy bundle is redirected from on surface to another, the transform matrix between the emission surface and reference coordinate is used to find the new direction of energy bundle and destination surface. Then on destination surface, another transform matrix is used to find incoming direction and new redirected direction. This process repeats until the remained energy of the bundle is less than the pre-defined extinction criterion.

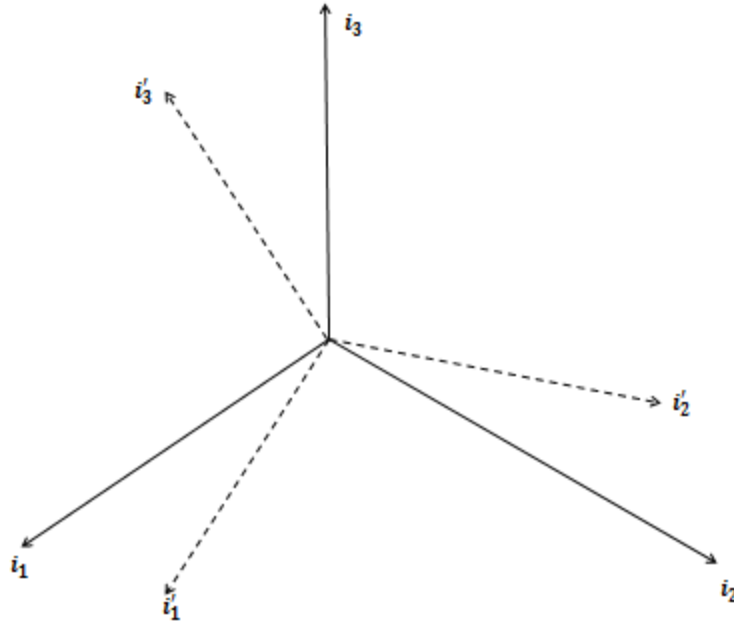
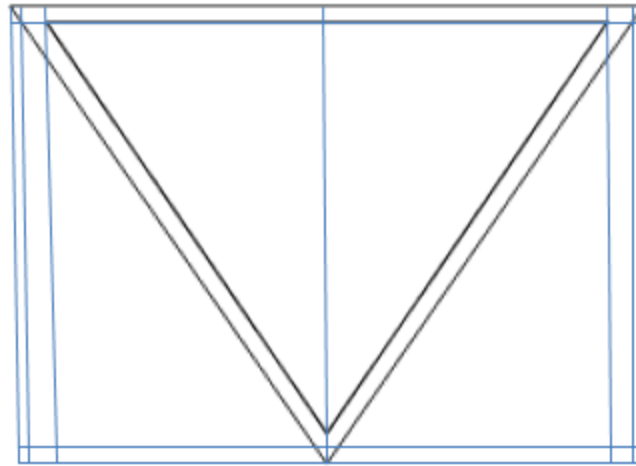


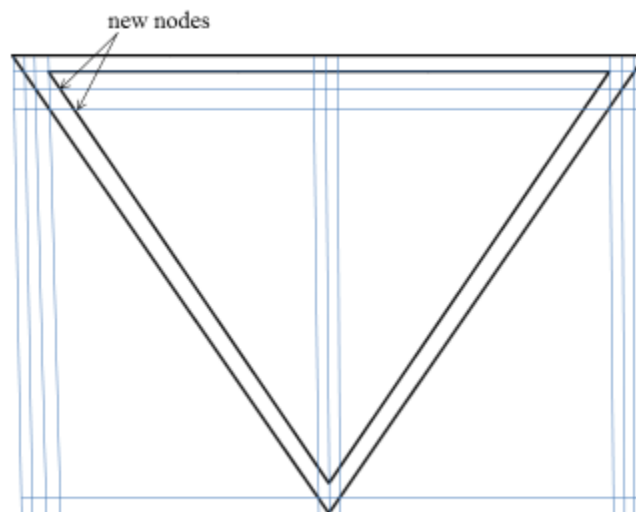
Fig 2.6 Transformation of coordinates in 3D

2.4 Mesh Generation

In order to place all interfaces at mesh boundaries, non-uniform triangular meshes are adopted. The first step is to define a brief frame that has all interfaces on boundaries, then the cross points of frame and mode boundary become new nodes. In order to fit the new nodes, a horizontal frame and a vertical frame has to cross at the node. Then more cross points are created, followed by more horizontal and vertical frames. Thus the triangular mesh is automatically formed and the grid size can be easily calculated from the dimensions of the model. A brief plot of mesh generation process is shown in Fig 2.7.



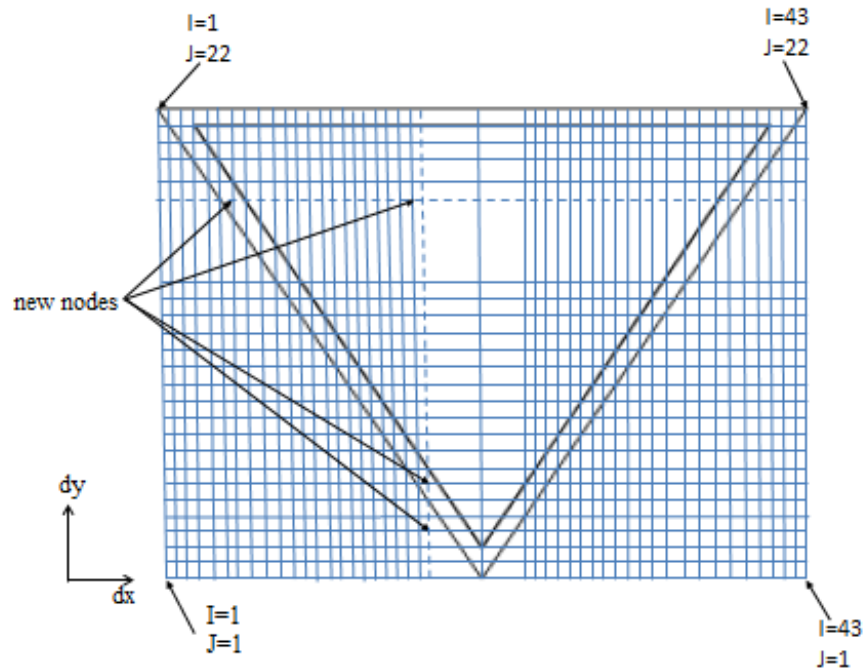
(a) Initial outline



(b) New nodes generated at cross points

Fig2.7 Mesh generation algorism

Fig 2.7(continued)



(c) Generate complete meshes

Fig2.7 Mesh generation algorism

2.5 Labeling Elements

2.5.1 Define points of the mesh

The method of labeling points comes from ref. [28]. There are $IDIM$ points per row and $JDIM$ points per column. Each node is defined by a set of index (I, J) signifying its coordinate in x and y direction.

2.5.2 Define edges of the mesh

Each edge is a joint of two adjacent node points, and there are three ways of joint that need to be defined separately. Each edge is defined by its joint type and an index of a

point. For a horizontal edge, its index is simply its left end node index, while for a vertical edge, the index is its lower end node index. For a diagonal edge, its index is the lower left corner node index of the rectangular element the diagonal edge belongs to, as shown in Fig 2.8 below. So the total number of horizontal, vertical and diagonal edges is $(IDIM - 1) \cdot JDIM$, $IDIM \cdot (JDIM - 1)$, and $(IDIM - 1) \cdot (JDIM - 1)$, respectively. A flag parameter *NDISP* is added to each edge to define interface type.

2.5.3 Define triangles of the mesh

We can see that in the two cases shown in Fig 2.8, the distribution of triangles inside rectangular cells is different. When $I+J$ is even ($MOD(I + J, 2) = 0$), triangles 1 and 2 are in the lower right and upper left corners of the rectangular cell. When $I+J$ is odd ($MOD(I + J, 2) = 1$), triangles 1 and 2 are in the lower left and upper right corners of the rectangular cell. Each boundary in the grid is assigned a different *IW* value from 1 to 5, for convenience in the ray tracing process that follows. A flag parameter *INDGWC* is added to each triangle defining the medium of the triangle or whether this triangle is blocked in the model being studied. Fig 2.9 gives a list of the parameters and their settings.

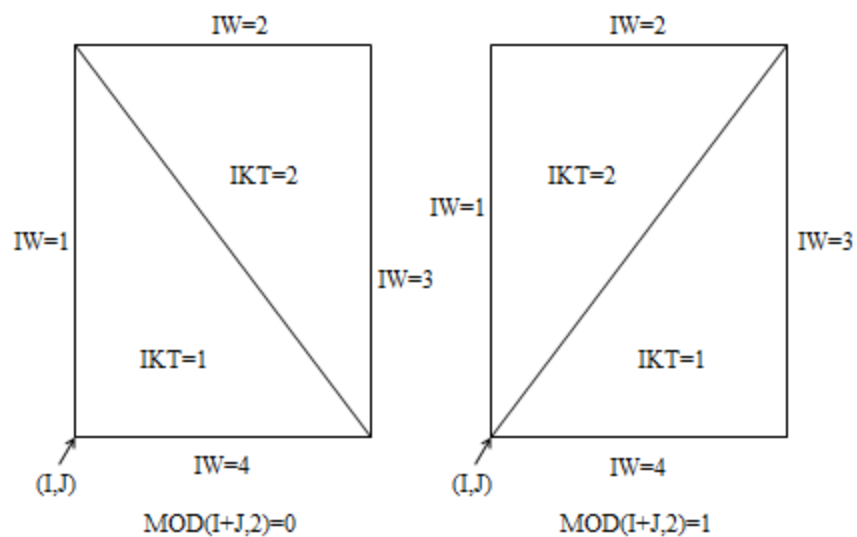


Fig 2.8 Labeling inside each element

INDGWC =	NDISP =
0 ----- BLOCKED	0 ----- INTERNAL EDGE
1 ----- GLASS	1 ----- GLASS-AIR
2 ----- WATER	2 ----- GLASS-WATER

INDABS=

0 ----- IN TRANSITION

1 ----- ABSORBED

Fig 2.9 Flags used in program

2.6 Program Flow Chart

The flow chart of the program is given in Fig 2.10 below. The meaning of each variable is given in nomenclature part of this thesis.

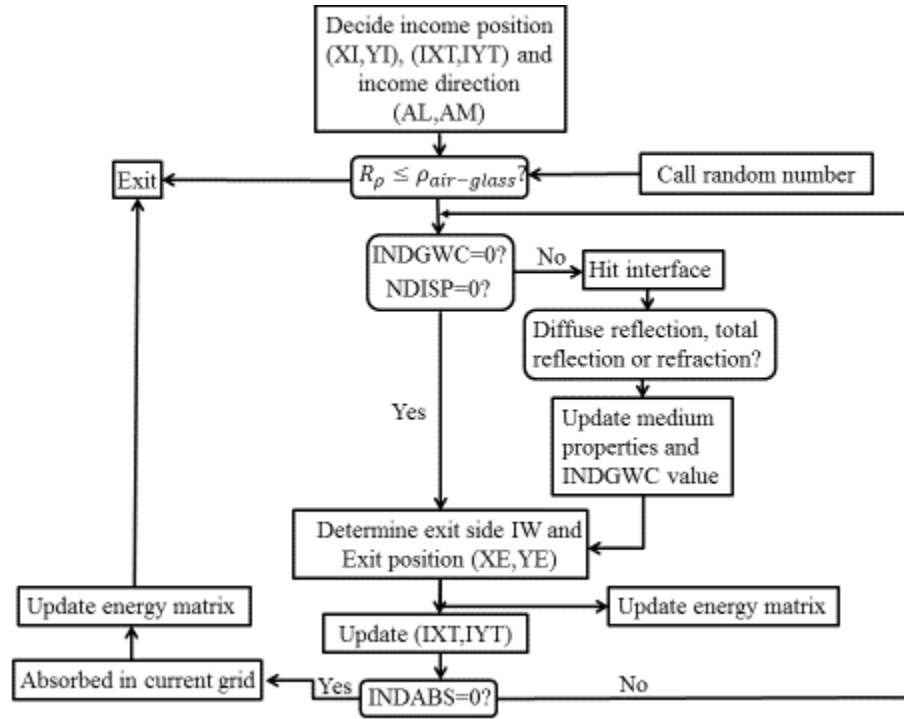


Fig 2.10 Flow chart of FORTRAN program

Chapter 3

Solar Irradiation Data

3.1 The Solar Constant

The *Total Solar Irradiation* (TSI) is the sum of the beam and the diffuse radiation [5] that arrives at the outermost layers of the atmosphere. And the *solar constant* E_{sc} is the long-term average of TSI. The solar constant is in fact not a constant, and it varies periodically, according to ref. [5], with sunspot activities. The effect of sunspot activities on the extraterrestrial radiation must be evaluated before taking E_{sc} as a constant throughout this thesis.

The speculation of solar constant variability can be dated back to over a century ago, and climate modelers have observed the significant variation of long term trends in solar constant [29]. The first reported measurement of solar constant is given by Vonder Haar (1968), data measured from earth orbiting satellites. More on zonal and geographical asymmetries of solar constant can be found in ref. [30]. Fig 3.1 provides illustration of

effect of sunspot numbers on solar constant, as a function of time between the year 1978 and 2003, the solar constant value of which corresponds to the standard value 1366.1 W/m^2 . We can also see in Fig 3.1 that there are only small variations with different periodicities related to sunspot activities, thus it's reasonable to take solar constant as a constant, for a certain day of the year, throughout this thesis without loss of accuracy.

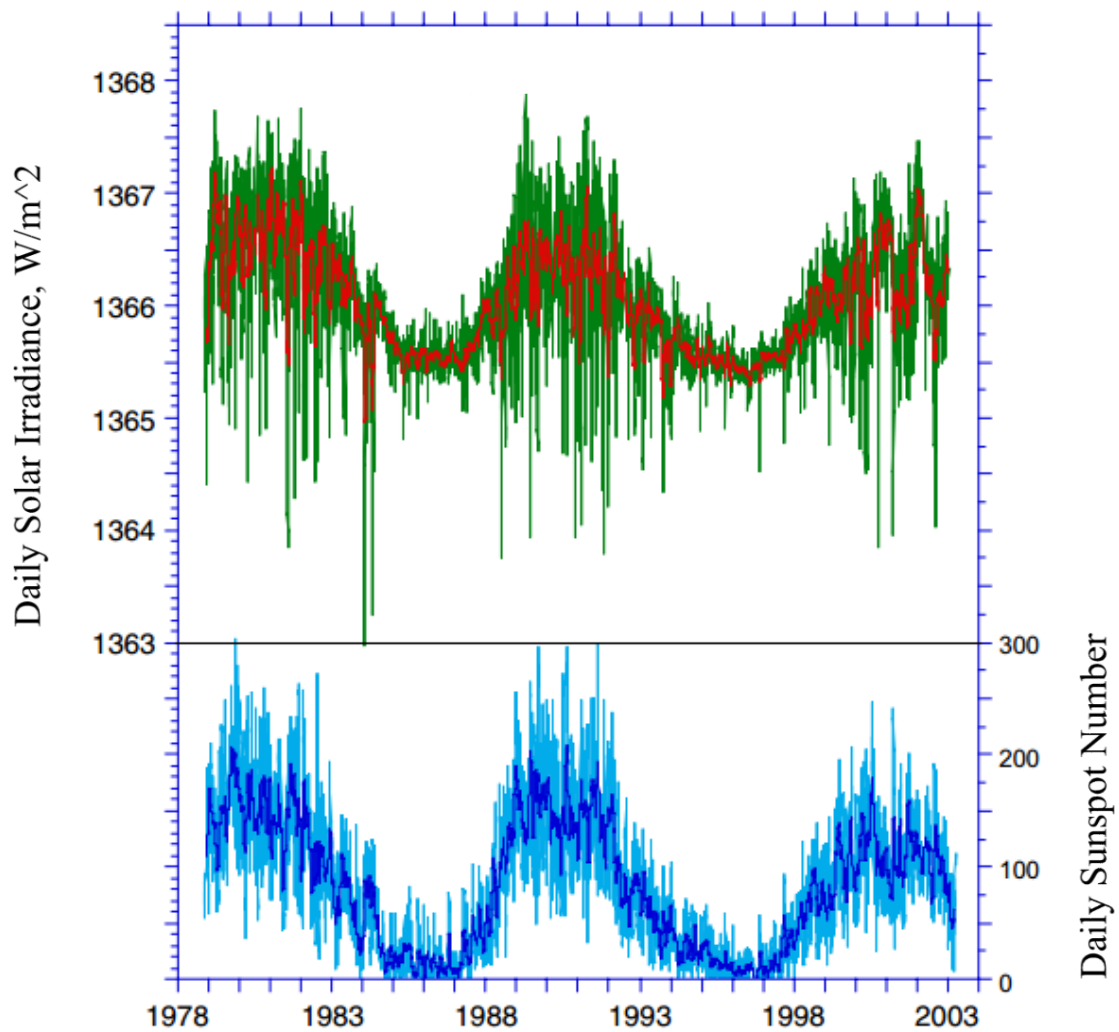


Fig 3.1 Daily total solar irradiance and daily sunspot number for the period 1978-2003 [31]

According to ref. [32], the standard value of extraterrestrial solar constant E_{sc} is given as:

$$E_{sc} = 1366.1 \text{ W/m}^2. \quad (3-1)$$

Variation of the earth-sun distance leads to variation of extraterrestrial radiation flux in the range of $\pm 3\%$, and the dependence of extraterrestrial radiation on time of year, according to ref. [5], is given by equation:

$$E_{on} = E_{sc} \left(1.0 + 0.033 \cos \frac{360n}{365} \right), \quad (3-2)$$

where E_{on} is the daily extraterrestrial irradiation, measured on the plane normal to the radiation on the n th day of the year. Other equations defining extraterrestrial irradiation can be found in ref. [33] and [34].

3.2 Air Mass (AM):

Air mass measures the ratio of the optical thickness of the atmosphere through which beam radiation passes to the optical thickness if the sun were at the zenith. The condition $AM = 0$ signifies extraterrestrial spectrum. The standard extraterrestrial spectrum data used here is provided by American Society for Testing and Materials in 2000 (ASTM E-490), as *Standard Solar Constant and Zero Air Mass Solar Spectral Irradiance Tables*. The integrated spectral irradiance of ASTM E-490 corresponds to the solar constant accepted by the space community, $E_{sc} = 1366.1 \text{ W/m}^2$. Besides the ASTM standard spectra we use, the *1985 Wehrli Standard Extraterrestrial Solar Irradiance Spectrum* is also frequently cited as the extraterrestrial solar spectral irradiance distribution.

The combination of different extinction processes in the atmosphere forms measurement of air mass, and the spectral dependent properties of complex components in the atmosphere explains for the spectral dependent AM values. If these factors are to be

considered while calculating band averages, the averages should be weighted by solar spectral irradiance for accuracy.

In the data set used for calculation, a single air mass value, $AM = 1.5$, is used for simplification without loss of obvious accuracy. This is also the widely accepted

Fig 3.2 gives comparison of extraterrestrial radiation, normalized blackbody radiation with a source temperature of 5762 K, clear sky $AM=1.0$ with and without molecular absorption [35].

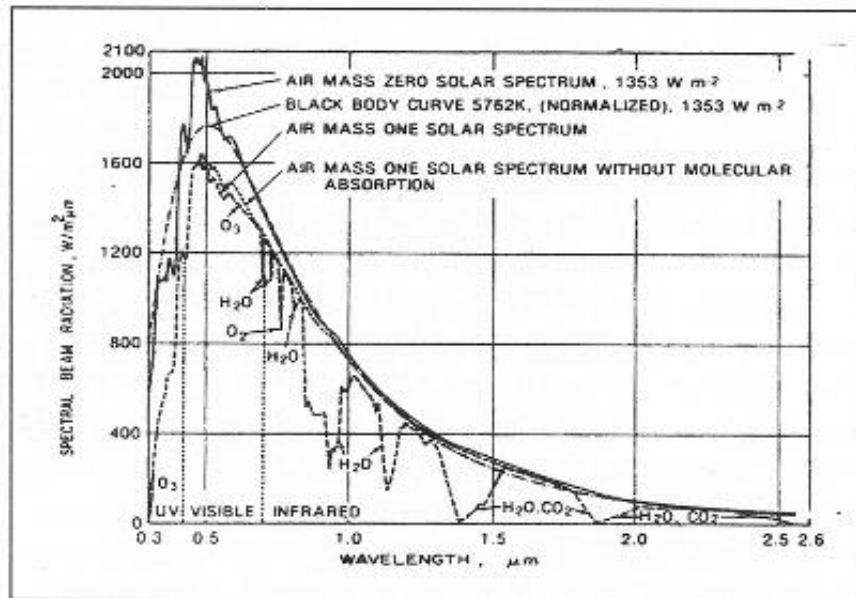


Fig 3.2 Attenuation of solar energy by the atmosphere (Thekaekara, 1974)

3.3 Atmospheric extinction of Solar Radiation

The atmosphere is composed of gases, water vapor and aerosols. Nitrogen (78.1%) and oxygen (20.9%) are main atmospheric gases with constant concentrations [36], while concentrations of other atmospheric gases and components such as water vapor, ozone

and aerosols vary according to time and space [37]. Air molecules mainly contributes to absorbing the solar radiation, while clouds, consisting of mainly minute particles of liquid water, ice, or both, as well as some large particle impurities [38], are the main attenuators of scattering and absorption [39]. Different components affect the absorption process on different spectral bands. O_2 and ozone are responsible for absorption below 290 nm, while carbon dioxide and water vapor absorb the infrared band, which contributes greatly to temperature on earth [40].

As to scattering process, smaller particles mainly affect visibility while larger particles contribute to anisotropy part of scattering [41]. The scattering process is also influenced by cloud cover condition. According to [37], for clear days, the scattering is mainly directional scattering due to turbidity increased by high concentration of aerosols, while for cloudy days, the higher probability of precipitation increases the accumulation of aerosols favoring uniform scattering. The overall optical air mass is expressed as a multiple of optical thickness of several attenuators, and the accurate approximations can be found in [42]. A brief plot of atmospheric attenuation is given in Fig 3.3 on next page, and the values displayed in the figure are for $AM = 1.0$ case.

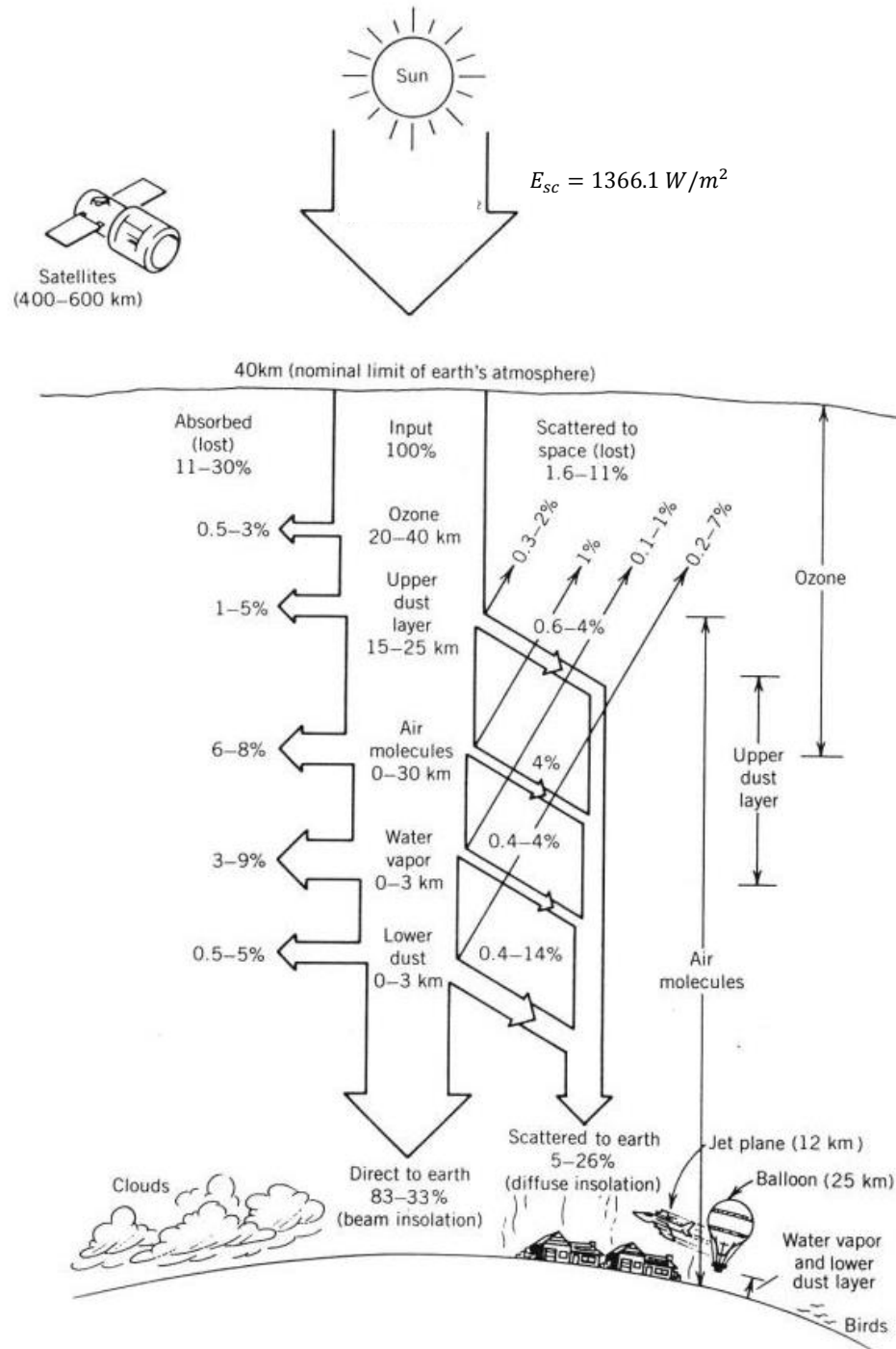


Fig 3.3 Clear sky absorption and scattering of incident solar energy [43]

In this thesis, atmospheric extinction is composed of Rayleigh Scattering, ozone absorption, Nitrogen dioxide absorption, uniformly mixed gas absorption, incremental

precipitable water absorption, and aerosol extinction. All these attenuators are discussed in detail below. Thus, the direct beam irradiance received at ground level by a surface normal to the sun's rays at wavelength λ is defined by

$$E_{bn\lambda} = E_{on\lambda} T_{r\lambda} T_{o\lambda} T_{n\lambda} T_{g\lambda} T_{w\lambda} T_{a\lambda} \quad (3-3)$$

where $E_{on\lambda}$ is the spectral extraterrestrial irradiance, and $T_{r\lambda}$, $T_{o\lambda}$, $T_{n\lambda}$, $T_{g\lambda}$, $T_{w\lambda}$, $T_{a\lambda}$ are optical thicknesses for different extinction processes that will be introduced in this section.

Besides the attenuators listed above, the absorption and scattering caused by pollutants in modern cities can also lead to relative attenuations of over 27%, 17% and 16% in ultraviolet, visible and near-infrared solar spectrum respectively, compared to clear atmosphere [44]. More on radiative perturbation caused by pollutants can be found in [45] and [46]. Localized factors such as atmospheric pollutants (including aerosols and greenhouse gases) and cloud cover conditions are not considered in this thesis, yet they appear for completeness purpose.

The data set used in this thesis comes from ASTM Standard G173-03 [47], the spectra of which are based on version 2.9.2 of the Simple Model of the Atmospheric Radiative Transfer of Sunshine (SMARTS) code developed by Christian Gueymard.

3.3.1 Rayleigh Scattering transmittance ($T_{R\lambda}$):

Interacting with a particle may change the path direction of an energy bundle. This can take place in three ways: diffraction, refraction, and reflection. All the three processes together are known as the *scattering* of radiation [10]. The *size parameter* is defined as

$$a = \frac{2\pi r}{\lambda} \quad (3-4)$$

where r is the effective radius of the particle. Scattering are divided into three categories according to the value of size parameter:

- a. $a \ll 1$. *Rayleigh Scattering*, named after Lord Rayleigh. Lord Rayleigh discovered the scattering model that for very small particles, scattering goes as forth power of the wavelength [48], and a complete list of his great works on electromagnetic wave propagation can be found in [49]. For atmospheric scattering, most air molecules have relatively very small radius. Thus Rayleigh scattering composes the most of atmospheric gases scattering. Rayleigh scattering is well-known for explaining why the sky is blue.
- b. $a = O(1)$. *Mie Scattering*, named after Gustav Mie, who developed model for interaction between electromagnetic waves and particles with comparable sizes [50].
- c. $a \gg 1$. This is the case of interaction between radiation and surface, and the results are related to the geometry of the enclosure.

The scattering coefficient of Rayleigh scattering can be calculated from equation [51]:

$$\sigma = \frac{24\pi^3}{N_0^2 \lambda^4} \left(\frac{n_0^2 - 1}{n_0^2 + 2} \right)^2 \left(\frac{6 + 3\delta}{6 - 7\delta} \right) \quad (3-5)$$

where N_0 is the molecular density ($2.547305 \times 10^{25} m^{-3}$ at $15^\circ C$), n_0 is the refractive index of air, λ is the wavelength, and δ is the depolarization ratio.

Then optical depth of Rayleigh scattering can be obtained through equation (3-6) as:

$$\tau_{R\lambda} = \sigma \frac{PA}{m_a g} \quad (3-6)$$

$$= 24\pi^3 \frac{PA}{N_0^2 \lambda^4 m_a g} \left(\frac{n_0^2 - 1}{n_0^2 + 2} \right)^2 \left(\frac{6 + 3\delta}{6 - 7\delta} \right) \quad (3-7)$$

where P is the pressure, A is Avogadro's number, m_a is the mean molecular weight of the air which depends on composition of air, and g is the acceleration of gravity, the value of which can be accurately calculated from equation given in ref. [52]. The depolarization term $\left(\frac{6+3\delta}{6-7\delta} \right)$ accounts for the most uncertainty, and it depends only on the gas mixture. To calculate, the full spectrum is divided into discrete bands with various band widths based on equivalent distribution of energy among bands. Based on data provided in ref. [51], Rayleigh optical depth $\tau_{R\lambda}$ can be readily plotted out as a function of wavelength, as shown in Fig 3.4. The data is measured for dry air containing 360 ppm CO_2 , at sea level altitude (45° latitude), under standard pressure.

Optical depth is related to transmittance by equation:

$$T_{R\lambda} = e^{-\tau_{R\lambda}}. \quad (3-8)$$

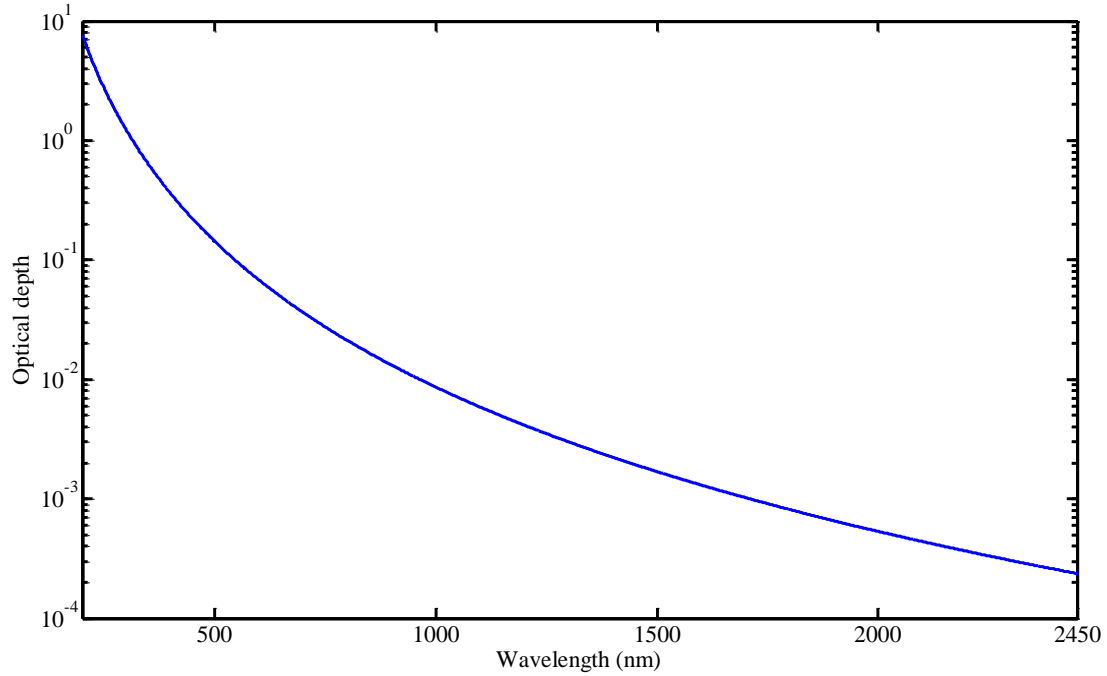


Fig 3.4 Rayleigh optical depth

3.3.2 Ozone Transmittance ($T_{o\lambda}$):

The Beer's law can be used to describe ozone transmittance:

$$T_{o\lambda} = \exp(-m_0 u_0 A_{o\lambda}), \quad (3-9)$$

where m_0 is the optical mass, u_0 is reduced path length as previously described, and $A_{o\lambda}$ is spectral absorption coefficient. Equations defining values of $A_{o\lambda}$ can be found in [53]. Based on data from [54], which is a combination of work from [55], [56], [57], [58], [59] and [60], a plot of ozone absorption coefficient over range 200 – 2550 nm is given in Fig 3.5 below. All values are band-averaged results weighted by spectral irradiation intensity. The sharp peak in the figure indicates that ozone absorption is especially spectral selective. Density variations of ozone in atmosphere are proven to affect the amount of

solar UV radiation received on the ground. According to [61], ozone reduction of 1% leads to a $1.25 \pm 0.20\%$ increase in erythemally active UV irradiance.

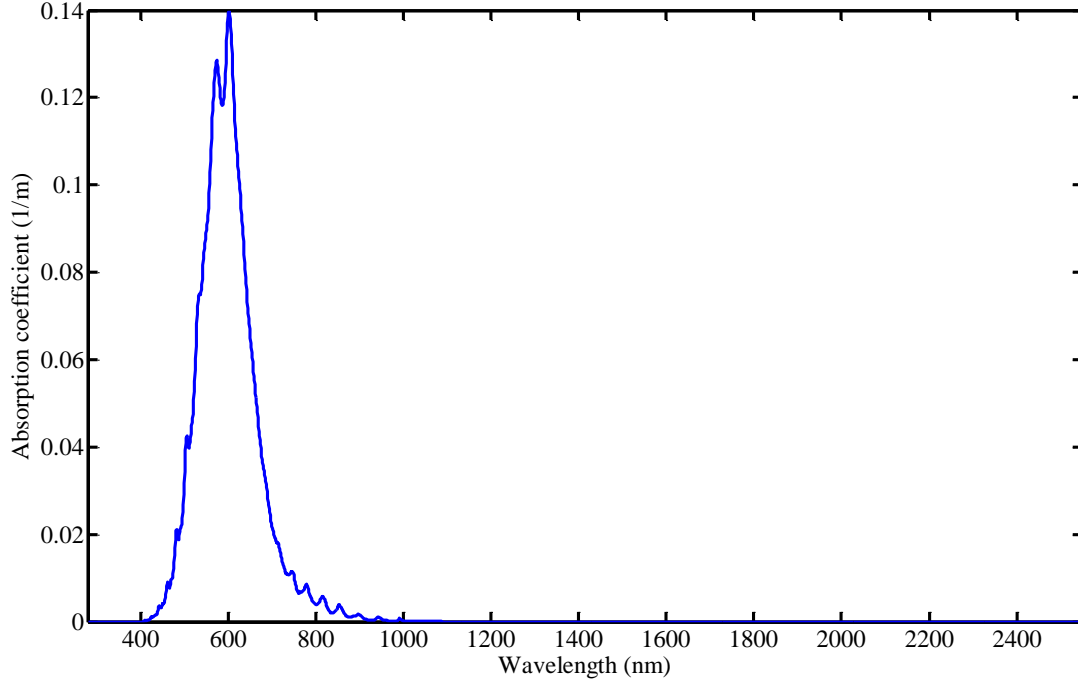


Fig 3.5 Ozone absorption coefficients

3.3.3 Nitrogen Dioxide Transmittance ($T_{n\lambda}$):

NO_2 transmittance can also be modelled by Beer's law:

$$T_{n\lambda} = \exp(-m_n u_n A_{n\lambda}), \quad (3-10)$$

where m_n is the NO_2 optical mass, u_n is the path length, and $A_{n\lambda}$ is the spectral absorption coefficient. The values of spectral absorption coefficient $A_{n\lambda}$ can be found in works such as [62] and [63]. Band averaged absorption cross-sections weighted by solar spectrum are available in [64].

3.3.4 Uniformly Mixed Gas Transmittance ($T_{g\lambda}$):

The main constituents of mixed gas are O_2 and CO_2 .

For mixed gas, a reduced pathlength has been developed to replace the real inhomogeneous path:

$$u_g = \int_z^\infty \left(\frac{p(h)}{p_0} \right)^n \left(\frac{T_1}{T(h)} \right)^m \left(\frac{\rho_a(h)}{\rho_{a0}} \right) dh, \quad (3-11)$$

where (h) , $T(h)$, $\rho_a(h)$ represents the pressure, temperature and air density at level h , $p_0 = 1013.25 \text{ mb}$, $T_1 = 288.15 \text{ K}$, $\rho_{a0} = 1.225 \text{ kg/m}^3$ are standard properties taken as constant, and n and m are absorber parameters. The values of n and m can be found for different gases and conditions by [65], and numerical methods leading to n and m values as well as discrete form of empirical transmittance function can be found in [66]. The equation of u_g can be fitted into a more compact form, where only pressure and temperature are explicitly expressed:

$$u_g = c_0 P^{c_1} \theta^{c_2} \quad (3-12)$$

where $P = p/p_0$, and $\theta = 288.15/T$ are pressure and temperature corrections, respectively. The values of the coefficients are: $c_0 = 4.9293 \text{ km}$, $c_1 = 1.8849$, $c_2 = 0.1815$ for O_2 and $c_0 = 4.8649 \text{ km}$, $c_1 = 1.9908$, $c_2 = -0.697$ for CO_2 .

According to [65] and [67], the mixed gas transmittance is defined as:

$$T_{g\lambda} = \exp[-(m_g u_g A_{g\lambda})^a] \quad (3-13)$$

where $m_g = m_R$ is the gas optical mass, $A_{g\lambda}$ is the spectral absorption coefficient, u_g is again the reduced path length, and a is the exponent, taking value of 0.5641 for $\lambda < 1 \mu\text{m}$, and of 0.7070 on rest of the band.

3.3.5 Incremental Precipitable Water Vapor Transmittance ($T_{w\lambda}$):

Water vapor is the most important absorber of solar energy in the near infrared spectrum. Different approximation methods have been used to calculate water vapor absorption coefficients. Assuming water vapor to be perfect gas [68], the total amount of precipitable water vapor, w , can be obtained through integration:

$$w = \int_0^z \rho_v(z) dz \quad (3-14)$$

where z is the atmospheric column height and ρ_v is the absolute humidity at z , which can be determined from equation

$$\rho_v(z) = \frac{217 \times RH(z) \times e(z, T)}{T}, \quad (3-15)$$

where T is the observed absolute temperature, $RH(z)$ is the relative humidity, and $e(z, T)$ is the saturation water vapor pressure in millibars(mb). The values of $e(z, T)$ can readily be calculated via different methods provided in [69], [70], [71], [72], or [73]. Another interesting introduction on determination of the total precipitable water based on digital water-vapor image can be found in [74]. More details about calculating optical properties of water can be found in [75].

3.3.6 Aerosol Absorption ($T_{a\lambda}$):

Human activity has perturbed the earth's energy balance. The pollutant gases and aerosols have changed the composition and properties of our atmosphere. Loadings of industrial-produced aerosols have increased greatly over the past 150 years [46]. These

aerosols enhance solar radiation reflection by both scattering and increasing the reflectivity of clouds, and this process increases the path length of solar radiation while traveling through atmosphere. Thus in turn, more solar energy is converted into heat, the atmosphere is heated up. The main contributor of solar energy absorption is submicron carbon particles at solar radiation wavelengths [76]. A lot of study has been done on measurement of aerosol absorption coefficients, on both discrete bands and continuous spectra [77] [76] [78]. Since the optical thickness of aerosol is a local variable, it's not considered in this thesis.

3.3.7 Greenhouse Gases Absorption:

The emission of greenhouse gases coming from industry is also changing the composition of atmosphere. *Radiative forcing* is defined as the difference between incoming and outgoing radiation [79], measured in watts per square meter. Fig 3.6 below is a contour showing estimated worldwide radiative forcing values caused by greenhouse gases. Positive radiative forcing in the figure indicates net increase in Earth's energy budget. A more comprehensive introduction on greenhouse gases, ozone and aerosol radiative forcing can be found in ref. [80], along with time evolution of radiative forcing.

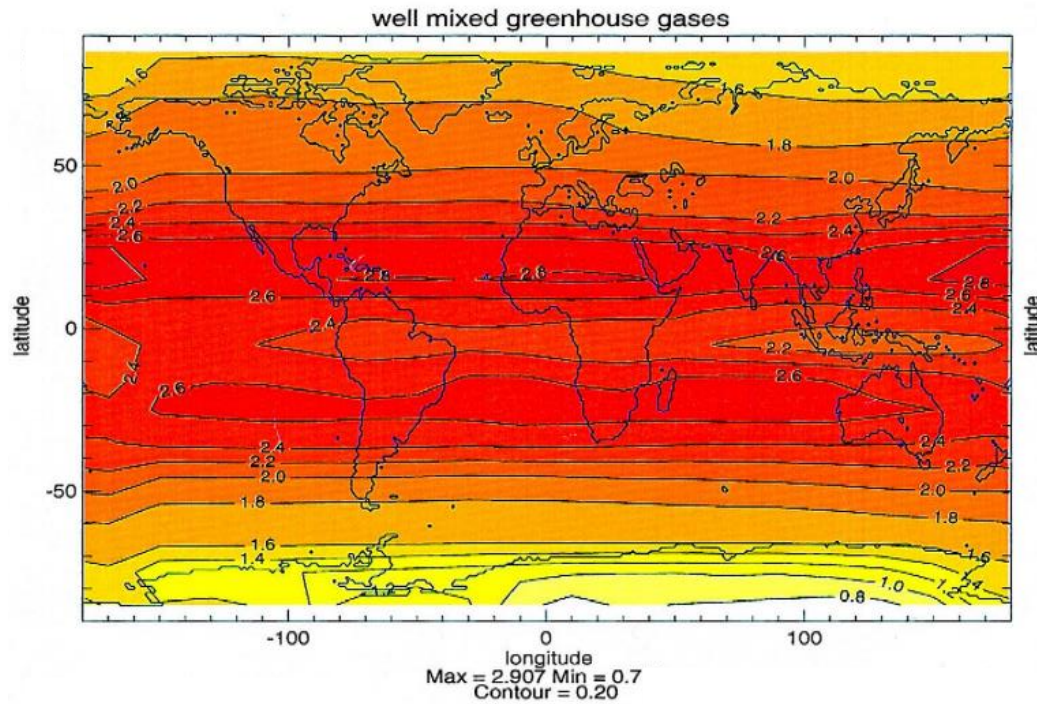


Fig 3.6 Spatial patterns of radiative forcing estimates due to greenhouse gases [81]

3.3.8 Radiative Forcing of Cloud Cover:

Clouds cover about 60% of the Earth's surface [82], and they are proven to modulate the global atmospheric extinction coefficient, through both scattering and absorption [83]. The first study on cloud radiative properties is conducted by the International Satellite Cloud Climatology Project (ISCCP) in ref. [84]. The contamination of aerosols makes the propagation of light through cloudy atmosphere more complicated [85]. A detailed and comprehensive study of radiation calibration considering cloud effects can be found in ref.[86]. However, real cloud can be simplified as a horizontally infinite homogeneous plan-parallel layer model [87] [88]. Then the extinction coefficient, for a given vertical coordinate z , is given by equation [83]:

$$\sigma_{\text{ext}} = N \int_0^{\infty} f(a) C_{\text{ext}} da \quad (3-16)$$

where N is the number of concentration particles, $f(a)$ is the size distribution of particles with radius a , and C_{ext} is extinction cross section, the values of which can be obtained through approximation methods provided in ref. [89], which is quite a good fit [90].

The data here we use comes from the Simple Model of the Atmospheric Radiative Transfer of Sunshine (SMARTS), which is a software developed to predict clear-sky spectral irradiances. This data needs to be modified by if the sky is cloudy and an obvious part of the solar radiation is blocked. These factors are taken into consideration in equation (3-16) below [5]:

$$\frac{\bar{H}}{\bar{H}_c} = \left(a + b \frac{\bar{n}}{\bar{N}} \right) \quad (3-17)$$

where \bar{H} = the monthly average daily radiation on a horizontal surface

\bar{H}_c = the average clear sky daily radiation for the location and month

a, b = empirical constants, varies locally

\bar{n} = monthly average daily hours of bright sunshine

\bar{N} = monthly average of the maximum possible daily hours of bright sunshine

The ratio $\frac{\bar{H}}{\bar{H}_0}$ is defined as *the clearness index*, \bar{K}_T .

The pioneering work coming up with empirical correlation between solar irradiation and clearness index was done by Liu and Jordan [91]. More detail on determining clearness

index can be found in ref. [92]. A comprehensive study on different models that are used to predict solar radiation is given in ref. [93].

3.4 Global Horizontal Irradiation (GHI)

3.4.1 Direct Normal Irradiation (DNI):

The solar radiation received from the sun without having been scattered by the atmosphere.

Integrated DNI value is 887.65 W/m^2 in the data set we use.

3.4.2 Diffuse Horizontal Irradiation (DHI):

The solar radiation received from the sun after its direction has been changed by scattering by the atmosphere (diffuse horizontal irradiation is sometimes called circumsolar irradiation in some references). Studies have shown that diffuse horizontal irradiation has a strong dependency with global horizontal irradiation and AM value [94].

3.4.3 Ground-reflected Irradiation:

The radiation received from the sun which is reflected back into the atmosphere after striking the earth. Ground-reflected radiation is usually negligible compared to DHI and DNI, so the global radiation here is said to be the sum of DHI and DNI only.

3.4.4 Global Horizontal Irradiation (GHI):

The sum of direct Normal irradiance, diffuse irradiation and ground-reflected radiation received on a horizontal surface. Global radiation is the radiation we are to use as total

source irradiation during calculation. The relation between circumsolar irradiation, ground-reflected irradiation and global horizontal irradiation can be expressed as:

$$GHI = DHI + DNI \cdot \cos(Z) \quad (3-18)$$

A brief plot to better illustrate direct normal irradiation, diffuse irradiation, ground-reflected irradiation and global horizontal irradiation is given in Fig. 3.7 below.

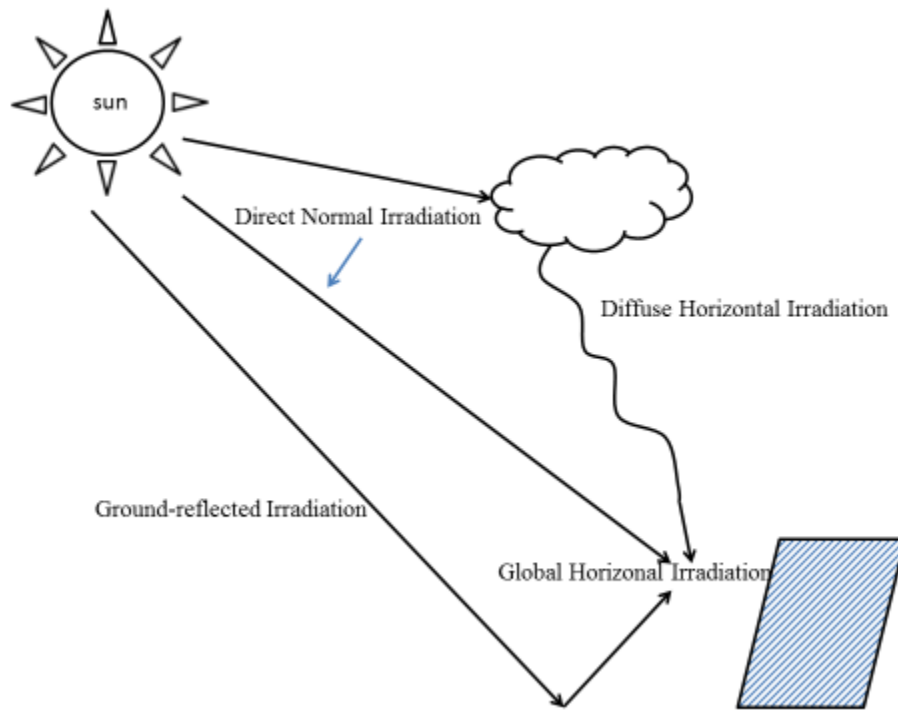


Fig 3.7 Components of Global Solar Irradiation

Integrated GHI equals 1007.806 W/m^2 in the data being used, which leads to a direct to global solar irradiation ratio of 0.88. We take this ratio as constant over full solar spectrum. In this thesis, only the direct solar irradiation part is considered, i.e., we only consider collimated solar irradiation. Thus in each case being studied, incoming direction is always a constant. In ref. [91], this ratio has been proved to be a constant all year around when ratio of global to extraterrestrial irradiation is greater than 0.75, which

applies in most cases. Comprehensive reviews on different solar radiation models defining solar radiation parameters can be found in ref. [95] and ref. [96].

The solar spectrum used in this thesis is the ASTM G-173-03 Standard Spectra, which is produced using most recent composite time series of total solar irradiance measurements and a solar constant of 1366.1 W/m^2 by Christian Gueymard [97]. The spectrum covers UV spectral region from 0.5 nm to 280 nm in 1 nm steps, from 280 nm to 400 nm in 0.5 nm steps, visible and part of near infrared from 400 nm to 1705 nm in 1 nm steps, steps of 5 nm from 1710 nm to 4000 nm, and variable steps beyond, up to 1000000 nm.

The target receiving surface norm points to the sun, which is not a horizontal surface but a surface with 41.81° elevation above horizon. The atmospheric conditions are the 1976 U.S. Standard Atmosphere defined in ref. [98].

Since we consider only the thermal and lighting effect of solar radiation, a truncated spectrum from 280 nm to 4000 nm is considered as full solar spectrum in this thesis, without loss of accuracy. A comparison of extraterrestrial, global and direct solar spectrum ($AM = 1.5$) is given in Fig 3.8 below. The unit of spectral solar irradiation is $\text{W/m}^2 \cdot \text{nm}$. We can see from the figure that different bands have different decay behaviors due to spectral dependence of atmospheric absorption.

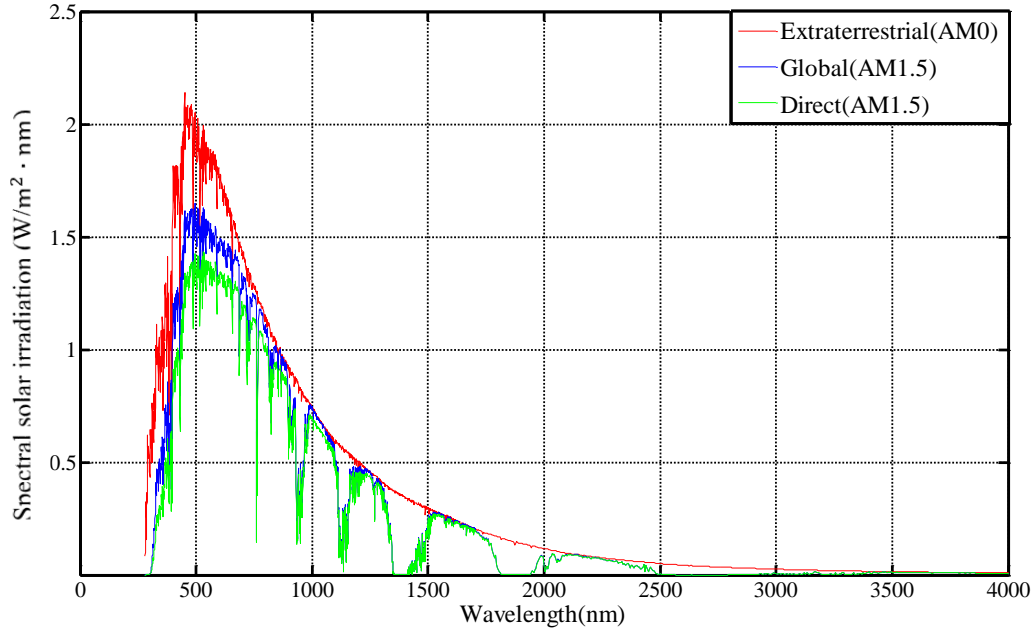


Fig.3.8 Spectral solar irradiation

3.5 Silica Glass Properties

Silica glass plays a very important role in modern buildings, such understanding the thermal properties of glass is very important in evaluating solar energy harvest in buildings. Glass material can be considered as an absorbing-emitting medium in the infrared region, and a transparent medium in the visible region [99].

3.5.1 Silica Glass Refractivity:

Spectral refractive index of silica glass is given by equation (3-19) from ref. [100]:

$$n = 1.5130 - 0.003169\lambda^2 + 0.003962\lambda^{-2} \quad (3-19)$$

Equation (3-19) is a simplified form of silica glass refractive index which fits experimental measurements to the third decimal. Ref. [101] provides full equations to

calculate a set of optical constants for common window glasses. Fig 3.9 shows spectral reflectivity of silica glass.

3.5.2 Silica Glass Absorptivity:

The absorption indices of silica glass can also be found in ref. [101], and the relationship between absorption index and absorptivity is defined by:

$$\kappa_{\lambda} = \frac{4\pi k_{\lambda}}{\lambda} \quad (3-20)$$

The spectral absorptivity of silica glass is given in Fig 3.10.

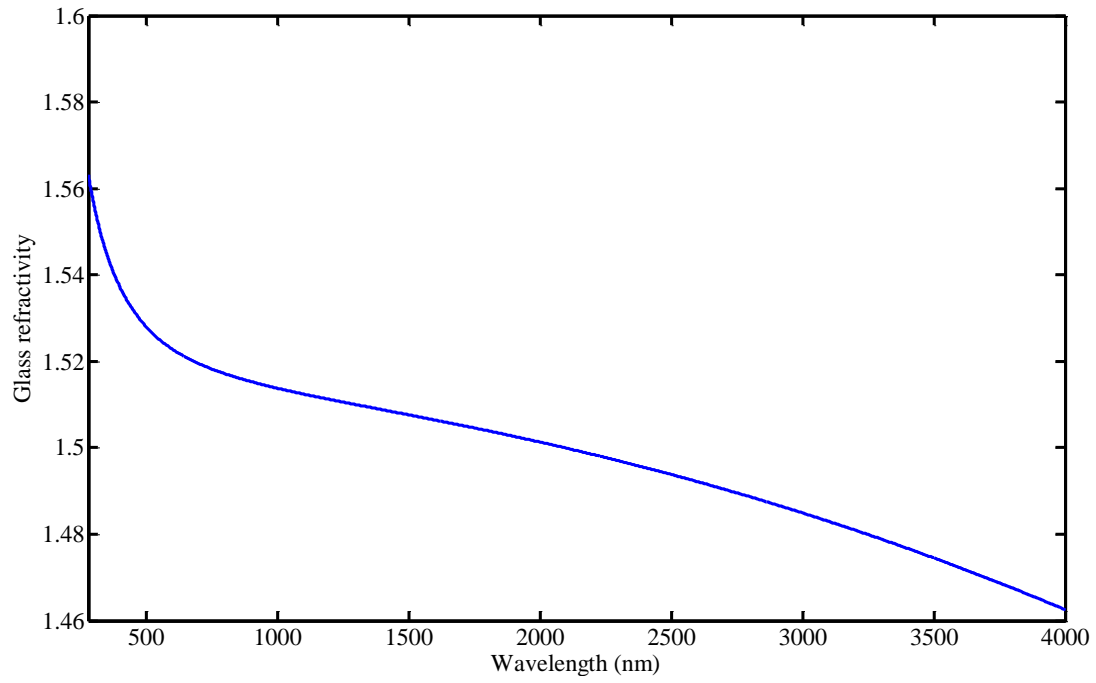


Fig 3.9 Silica glass refractivity

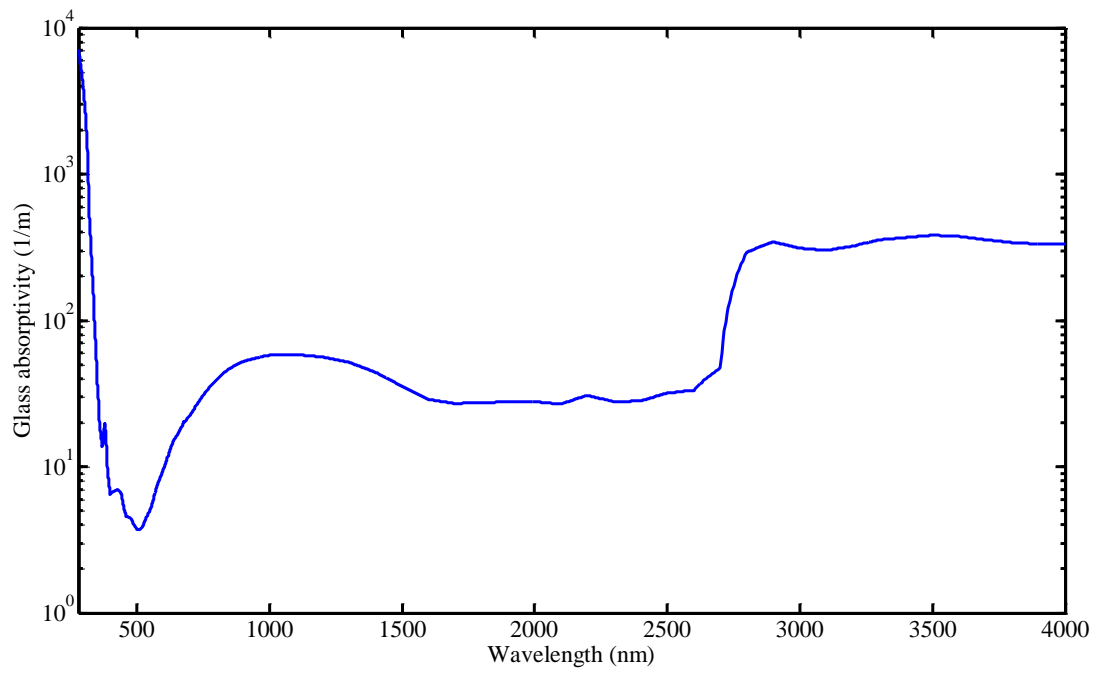


Fig 3.10 Silica glass absorptivity

3.6 Water Properties

The spectral properties of pure water can be found in ref. [102], which provides optical constants of water in the 200 nm to $200\text{ }\mu\text{m}$ region. The refractivity and absorptivity are plotted separately in Fig 3.11 and Fig 3.12 below. Refractivity is unitless and absorptivity is of unit m^{-1} .

3.6.1 Water refractivity:

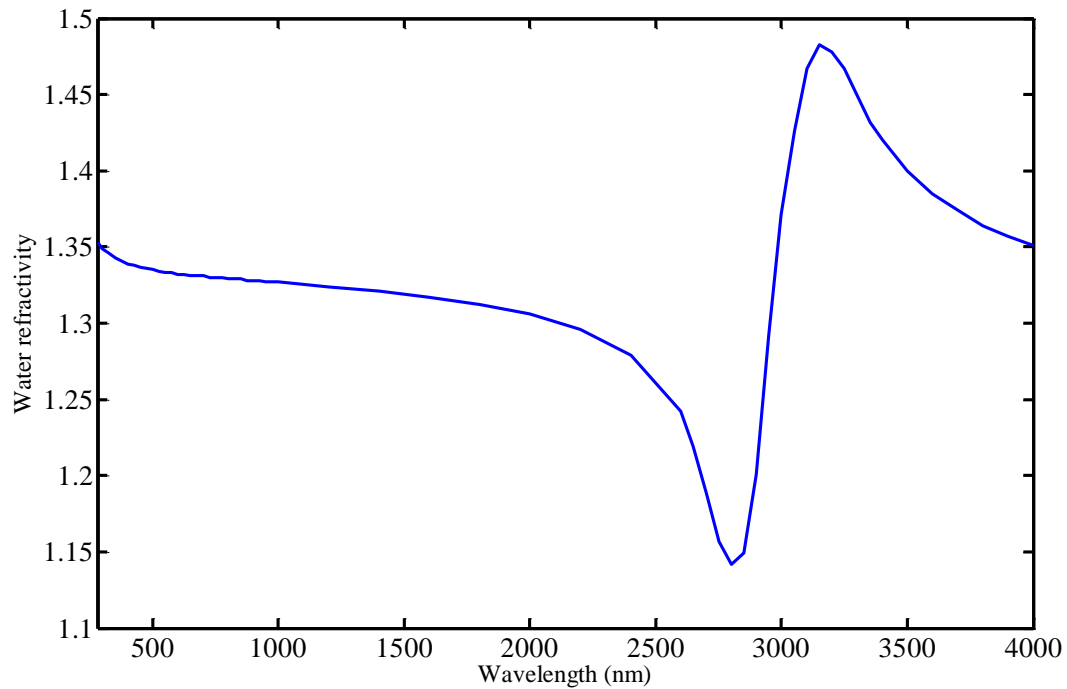


Fig 3.11 Water refractivity

3.6.2 Water Absorptivity:

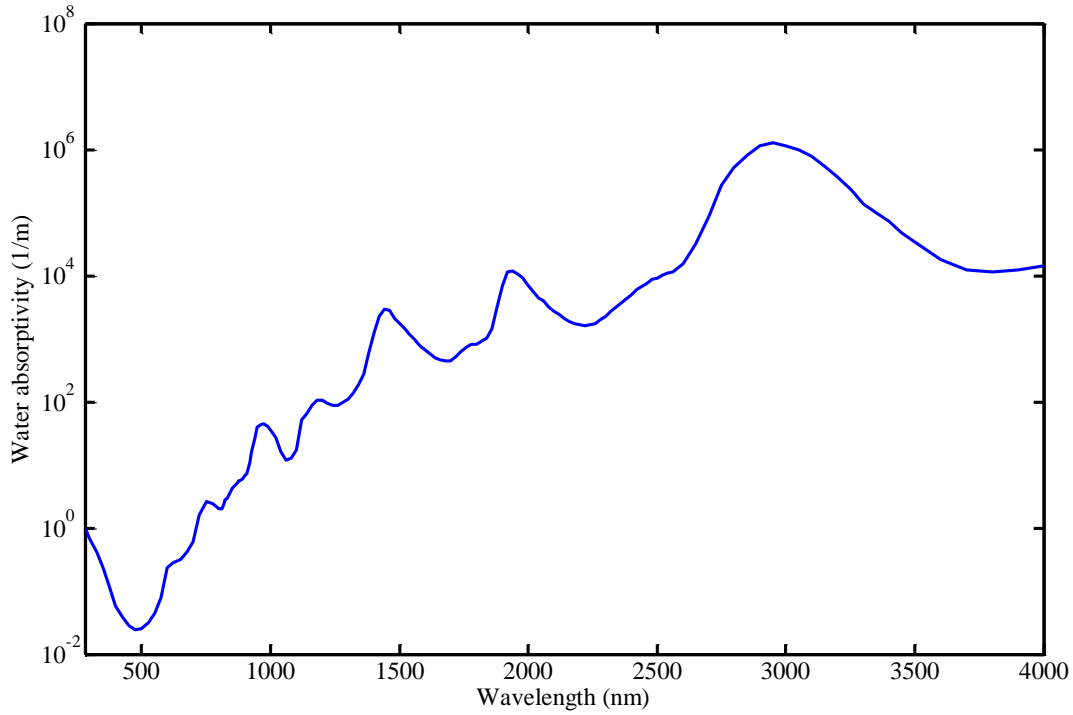


Fig 3.12 Water Absorptivity

3.7 Weighted Spectral Properties

All spectral properties used in the FORTRAN program are energy-weighted on each band.

3.7.1 Weighted Average:

The integral form of weighted average is defined as:

$$X = \frac{\int_{\Delta\lambda_i} x(\lambda_i) \cdot \text{RSL}(\lambda_i) \cdot w(\lambda_i) d\lambda_i}{\int_{\Delta\lambda_i} \text{RSL}(\lambda_i) \cdot w(\lambda_i) d\lambda_i} \quad (3-21)$$

where X is band-averaged property, $\Delta\lambda_i$ is band width of a certain band, $i=1, 2, \dots, n$, $x(\lambda_i)$ is spectral properties at each wavelength $\Delta\lambda_i$, $RSL(\lambda_i)$ is spectral response function, and $w(\lambda_i)$ is weight factor. Here we take $RSL(\lambda_i)$ as 1, and take spectral intensity $I(\lambda_i)$ as weight factor of spectral-dependent properties.

The integral form can be used when the spectral properties are continuous on the domain being studied. More options on modified weighted average method and band parameter determination, as well as comparisons between different options, can be found in ref. [103]. However, the spectral properties of water and glass we use are mostly discrete data sets, and the weighted average equation needs to be discretized.

3.7.2 Discretization:

The discretized form of weighted average equation can be written as:

$$X = \frac{\sum_m^n x(\lambda_i) \cdot I(\lambda_i) \cdot \Delta\lambda}{\sum_m^n I(\lambda_i) \cdot \Delta\lambda} \quad (3-22)$$

Here the weight factor $w(\lambda_i)$ is replaced by spectral intensity $I(\lambda_i)$.

To be more precise, we can use the composite Simpson's rule:

$$X = \frac{\frac{\Delta\lambda}{3} \cdot \sum_{j=1}^{\frac{n}{2}} [f(x_{2j-2}) \cdot I(x_{2j-2}) + 4f(x_{2j-1}) \cdot I(x_{2j-1}) + f(x_{2j}) \cdot I(x_{2j})]}{\frac{\Delta\lambda}{3} \cdot \sum_{j=1}^{\frac{n}{2}} [I(x_{2j-2}) + 4I(x_{2j-1}) + I(x_{2j})]} \quad (3-23)$$

After simplification, it can be written as:

$$X = \frac{\sum_{j=1}^{\frac{n}{2}} [x_{2j-2} \cdot I(x_{2j-2}) + 4x_{2j-1} \cdot I(x_{2j-1}) + x_{2j} \cdot I(x_{2j})]}{\sum_{j=1}^{\frac{n}{2}} [I(x_{2j-2}) + 4I(x_{2j-1}) + I(x_{2j})]} \quad (3-24)$$

where n is the number of data nodes included in each band and $\Delta\lambda$ is the bandwidth in the data set being used.

Since the bandwidth $\Delta\lambda$ of data sets from different sources is different, some redundant points in more compact data sets have to be removed in order to fit in the form of solar irradiation intensity data.

Chapter 4

Influence of Spectral Bands

4.1 Choice of Photon Number

The total energy coming in through each grid is split into NRAY photons each carrying equivalent portion of energy. As previously mentioned in chapter 2, the Monte Carlo method is a statistical method that requires a sample size large enough to guarantee accuracy. However, over-sized sample leads to extended calculation time without obvious improvement in accuracy. We need to find a suitable sample size among multiple possible choices that is time-saving and can meet the accuracy criteria.

To get a persuasive comparison, energy allocation at several representative sets of properties needs to be checked. At wavelength 550 nm, water absorptivity is of (-2) , glass absorptivity is of $O(1)$, and $\frac{\alpha_{glass}}{\alpha_{water}}$ is of $O(2)$. The other two wavelengths chosen also have representative properties with $\frac{\alpha_{glass}}{\alpha_{water}}$ of $O(-1)$ and $O(-4)$, respectively. The

properties and solar irradiation intensities at wavelengths 550 nm, 1550 nm and 3000 nm are given in table 4.1 below.

Table 4.1 Properties and intensities at wavelengths 550 nm, 1550 nm and 3000 nm

Wavelength (nm) Properties	550	1550	3000
n_{glass}	1.525	1.507	1.485
n_{water}	1.333	1.318	1.371
$\alpha_{glass} (m^{-1})$	5.03	32.06	3.11E2
$\alpha_{water} (m^{-1})$	4.48E-2	799.59	1.14E6
$E_{\lambda} (W/m^2 \cdot nm)$	1.5399	0.2699	7.8472E-3

Besides the three sets of spectral properties above, four NRAY values, 10^6 , 10^7 , 10^8 and 10^9 , are considered in each condition. The results are shown in figures below. Since log graph is used, all points with 0 value disappear, leading to cutoff in figures. For wavelength 1550 nm and 3000 nm, water absorptivities are of O(2) and O(6), separately, which explains the extremely fast decay and cutoff in Fig 4.2 and 4.3.

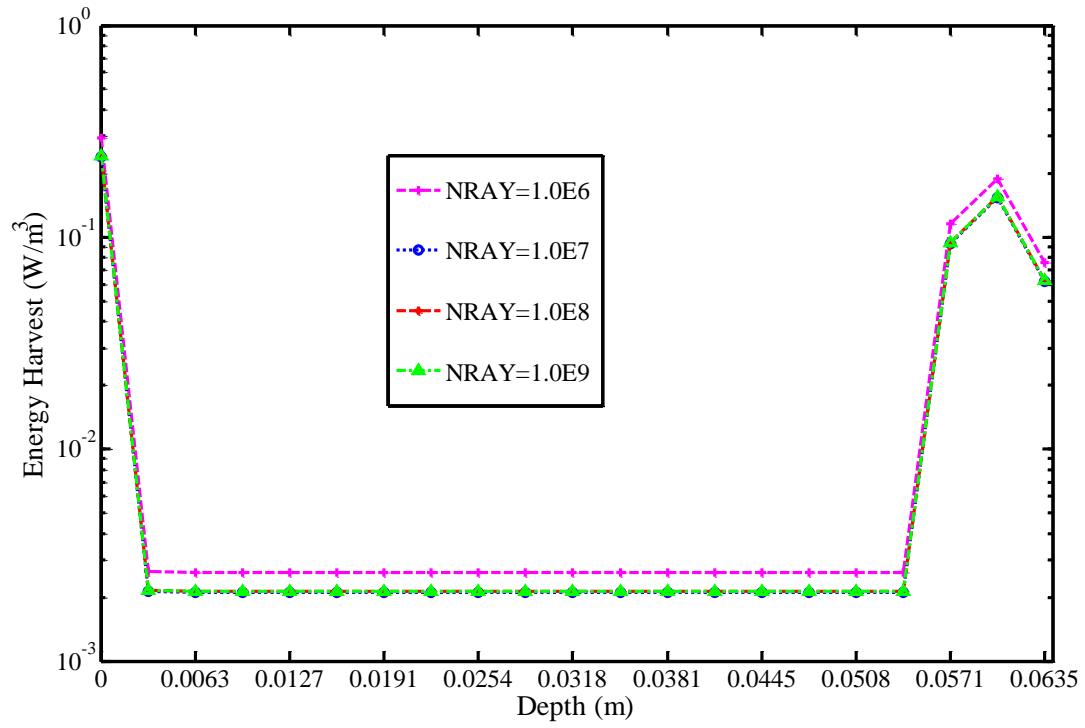


Fig 4.1 Centerline Energy harvest at wavelength 550nm

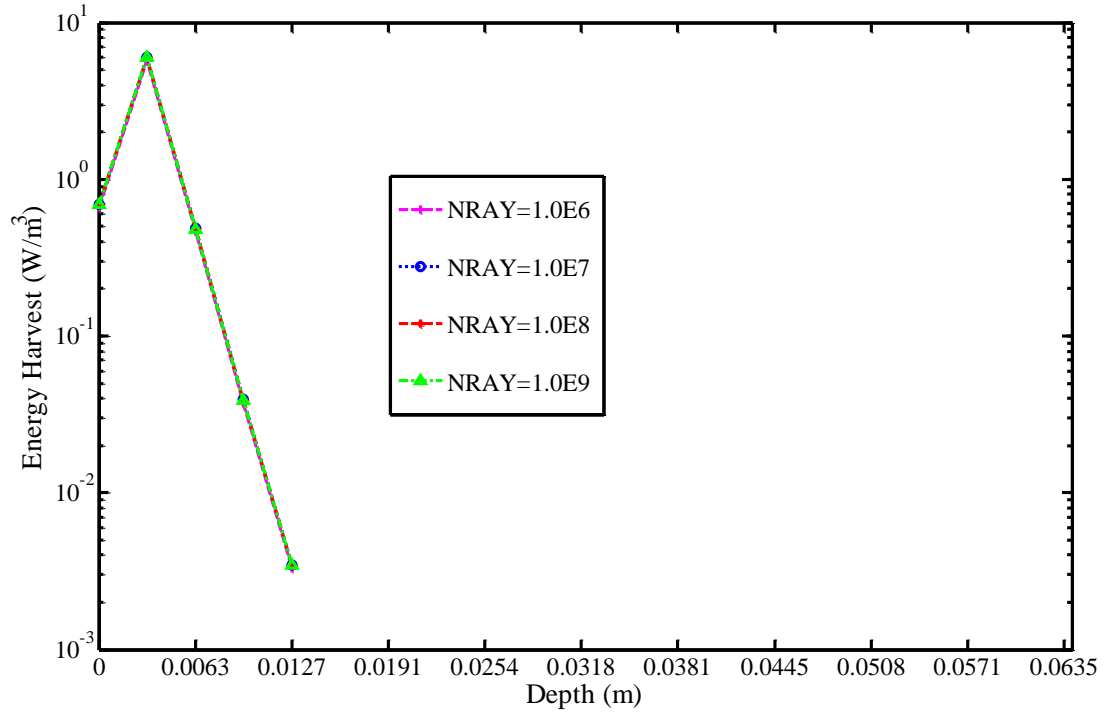


Fig 4.2 Centerline Energy harvest at wavelength 1550nm

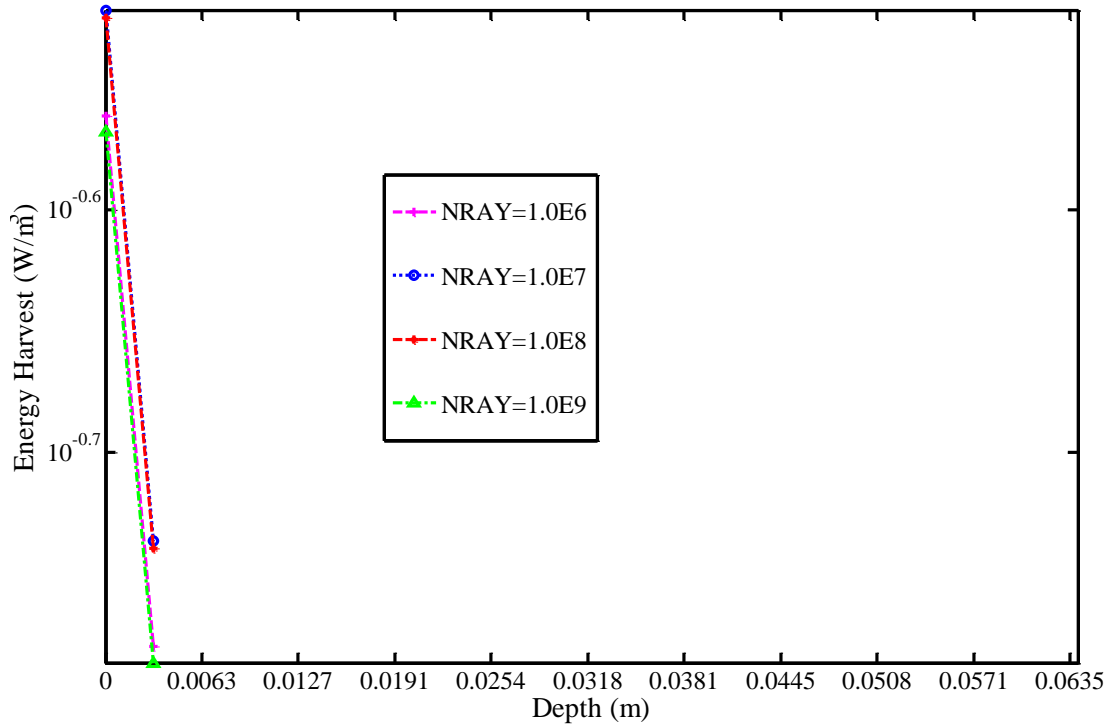


Fig 4.3 Centerline Energy harvest at wavelength 3000nm

From Fig 4.1 we can see that the energy harvest at centerline when $\text{NRAY}=10^6$ obviously deviates from the other three results, thus a sample size of 10^6 is too small to get an accurate result. In Fig 4.2, all the four sample sizes get consistent results. In Fig 4.3, the plots of 10^7 and 10^8 are quite close, while the plots of 10^6 and 10^9 deviate. This might be because when sample size is 10^9 , the incoming energy has been divided into too many small bundles, which leads to accumulative error that deviates the results from real energy allocation. While sample sizes of 10^7 and 10^8 are large enough to satisfy the sample size requirement of Monte Carlo method, and can avoid accumulative error and redundant computation at the same time. Besides, water and silica glass properties also affect accuracy. We can see that at wavelength 550 nm and 3000 nm, when the ratio

between water and silica glass absorptivities $\frac{\alpha_{glass}}{\alpha_{water}}$ are of $O(2)$ and $O(-4)$, the results of different sample sizes tend to diverge.

In the computation that follows, sample size of 10^8 is chosen. The next step is to choose how many bands the full solar spectrum should be divided into, so that spectral properties of medium and material can be taken into consideration.

4.2 Spectral Band Number Division

In order to choose band number, some investigation needs to be taken into the property profiles of water and glass provided in Chapter 3. Since band-averaged properties are used, we should select band regions in a way that property profiles are relatively smooth within each band so that the band-averaged values can represent the real property properly.

4.2.1 Variations of Silica Glass and Water Property Profiles:

Table 4.2 Vertex of silica glass and water property profiles

Wavelength (nm) Properties	Vertex1	Vertex2	Vertex3	Vertex4
Glass refractivity	750nm	N/A	N/A	N/A
Glass absorptivity (m^{-1})	400nm	1530nm	1970nm	2325nm
Water refractivity	2000nm	2800nm	3150nm	4000nm
Water absorptivity (m^{-1})	2650nm	2950nm	3800nm	4000nm

Another factor needs to be considered during band division is that each band should contain similar amount of energy to guarantee equivalent weight. So the bandwidth varies along full solar spectrum: in region with condensed energy, such as infrared region, the bandwidth is relatively narrower.

The full solar spectrum is divided into 3, 10, 20 and 40 spectral bands considering profile variation and energy distribution, and integral averages of properties are obtained on each band. Detailed divisions are listed in table 4.3-4.7. The last column from right to left in the tables is weight of each band.

1 Band (Full spectrum):

Table 4.3 1 band properties

Property Wavelength	n_{glass}	n_{water}	$\alpha_{glass} (m^{-1})$	$\alpha_{water} (m^{-1})$	Weight (%)
280~4000nm	1.5216	1.3307	35.0864	381.3735	100.000

3 Bands:

Table 4.4 3 bands properties

Property Wavelength	n_{glass}	n_{water}	$\alpha_{glass} (m^{-1})$	$\alpha_{water} (m^{-1})$	Weight (%)
280~600nm	1.5319	1.3367	28.8929	0.0858	33.586
600~1100nm	1.5176	1.3290	36.0783	12.494	46.788
1100~4000nm	1.5084	1.3206	47.5982	2473.5	19.626

10 Bands:

Table 4.5 10 bands properties

Property Wavelength	n_{glass}	n_{water}	$\alpha_{glass} (m^{-1})$	$\alpha_{water} (m^{-1})$	Weight (%)
280~400nm	1.5429	1.3421	102.5293	0.1929	4.575
400~500nm	1.5319	1.3369	5.3751	0.0322	13.922
500~600nm	1.5253	1.3333	5.6408	0.07	15.089
600~700nm	1.5211	1.3311	16.0014	0.3526	13.919
700~850nm	1.5178	1.3294	34.1597	2.4007	16.196
850~1100nm	1.5143	1.3268	54.6798	32.3981	16.673
1100~1530nm	1.5104	1.3230	52.0098	435.3489	10.088
1530~1700nm	1.5063	1.3166	29.3908	731.7093	4.018
1700~3000nm	1.5004	1.3005	30.3508	12595	4.780
3000~4000nm	1.4729	1.3972	351.6867	125250	0.740

20 Bands:

Table 4.6 20 bands properties

	Property Wavelength	n_{glass}	n_{water}	α_{glass} (m^{-1})	α_{water} (m^{-1})	Weight (%)
1	280~400nm	1.5429	1.3421	102.5293	0.1929	4.578
2	400~450nm	1.5343	1.3380	6.5916	0.0403	6.149
3	450~500nm	1.5299	1.3360	4.4101	0.0258	7.773
4	500~530nm	1.5271	1.3344	3.8295	0.0292	4.559
5	530~566nm	1.5253	1.3332	5.0490	0.0468	5.509
6	566~600nm	1.5236	1.3323	7.9275	0.1323	5.021
7	600~650nm	1.5219	1.3315	12.9215	0.2760	7.199
8	650~700nm	1.5203	1.3307	19.3064	0.4348	6.720
9	700~750nm	1.5189	1.3300	26.3851	2.0035	6.001
10	750~800nm	1.5177	1.3293	34.9274	2.3347	5.316
11	800~850nm	1.5167	1.3287	42.8651	2.9598	4.878
12	850~930nm	1.5156	1.3278	50.5189	7.4352	6.651
13	930~1000nm	1.5142	1.3267	56.3405	39.1301	3.556
14	1000~1100nm	1.5131	1.3258	58.0337	54.3222	6.465

	Property Wavelength	n_{glass}	n_{water}	α_{glass} (m^{-1})	α_{water} (m^{-1})	Weight (%)
15	1100~1200nm	1.5117	1.3245	57.1924	90.3071	3.152
16	1200~1300nm	1.5106	1.3233	54.0033	410.1431	4.305
17	1300~1530nm	1.5086	1.3205	42.4921	893.4837	2.631
18	1530~1700nm	1.5063	1.3166	29.3908	731.7093	4.018
19	1700~3000nm	1.5004	1.3005	30.3508	12595	4.780
20	3000~4000nm	1.4729	1.3972	351.6867	125250	0.740

40 Bands:

Table 4.7 40 bands properties

	Property Wavelength	n_{glass}	n_{water}	α_{glass} (m^{-1})	α_{water} (m^{-1})	Weight (%)
1	280~370nm	1.5459	1.3436	175.3724	0.2741	2.465
2	370~400nm	1.5392	1.3402	12.6989	0.0928	2.030
3	400~418nm	1.5362	1.3387	6.6426	0.0509	2.146
4	418~434nm	1.5343	1.3380	6.9023	0.0387	1.899
5	434~450nm	1.5326	1.3373	6.2805	0.0315	2.243
6	450~466nm	1.5312	1.3367	4.8093	0.0272	2.541

	Property Wavelength	n_{glass}	n_{water}	α_{glass} (m^{-1})	α_{water} (m^{-1})	Weight (%)
7	466~484nm	1.5298	1.3360	4.4557	0.0251	2.881
8	484~500nm	1.5286	1.3353	3.9545	0.0250	2.509
9	500~514nm	1.5276	1.3347	3.7208	0.0270	2.227
10	514~530nm	1.5267	1.3341	3.9284	0.0311	2.451
11	530~548nm	1.5259	1.3336	4.4105	0.0370	2.807
12	548~566nm	1.5250	1.3330	5.2975	0.0506	2.777
13	566~582nm	1.5240	1.3325	7.1211	0.0848	2.437
14	582~600nm	1.5232	1.3322	8.6563	0.1751	2.684
15	600~618nm	1.5225	1.3318	10.7808	0.2491	2.675
16	618~634nm	1.5218	1.3315	13.2685	0.2821	2.328
17	634~650nm	1.5213	1.3312	15.3588	0.3052	2.334
18	650~666nm	1.5208	1.3309	17.1635	0.3492	2.248
19	666~682nm	1.5203	1.3307	19.4444	0.4170	2.300
20	682~700nm	1.5198	1.3305	21.2542	0.5357	2.313
21	700~724nm	1.5192	1.3302	24.1409	1.8999	2.941
22	724~750nm	1.5186	1.3298	28.5397	2.1030	3.054
23	750~776nm	1.5180	1.3295	32.8266	2.5025	2.618

	Property Wavelength	n_{glass}	n_{water}	α_{glass} (m^{-1})	α_{water} (m^{-1})	Weight (%)
24	776~800nm	1.5174	1.3292	36.9404	2.1740	2.714
25	800~824nm	1.5169	1.3288	40.8048	2.3352	2.359
26	824~850nm	1.5164	1.3285	44.7769	3.5392	2.511
27	850~874nm	1.5160	1.3282	48.0565	4.9536	2.296
28	874~896nm	1.5156	1.3279	50.5921	6.0801	2.017
29	896~930nm	1.5151	1.3275	52.8901	11.060	2.292
30	930~1000nm	1.5142	1.3267	56.3405	39.1301	3.493
31	1000~1050nm	1.5134	1.3261	57.8741	45.9067	3.404
32	1050~1100nm	1.5128	1.3255	58.2190	64.0930	2.928
33	1100~1200nm	1.5117	1.3245	57.1924	90.3071	3.076
34	1200~1250nm	1.5109	1.3236	55.0663	266.7723	2.215
35	1250~1300nm	1.5103	1.3229	52.8308	568.2748	2.006
36	1300~1530nm	1.5086	1.3205	42.4921	893.4837	2.557
37	1530~1700nm	1.5063	1.3166	29.3908	731.7093	3.886
38	1700~2050nm	1.5037	1.3111	27.3000	2343.7	2.043
39	2050~3000nm	1.4979	1.2924	32.6871	20446	2.593
40	3000~4000nm	1.4729	1.3972	351.6867	125250	0.712

4.2.2 Energy Allocation of Different Bands:

Fig 4.4 gives centerline energy allocation under perpendicular irradiation ($\theta = 0$), with five different band divisions. The pink line signifying uniform band deviates obviously from the other four lines and decays very fast. This obvious deviation appears due to the fact that in uniform band case, the averaged water absorption coefficient in infrared spectrum (381.3735 m^{-1}) is much higher than the real water absorption coefficient in the same band domain (0.0858 m^{-1}), thus leading to over-estimation of energy harvest in grids.

By comparing different band division results, we can see that spectral consideration is necessary while dealing with highly spectral dependent irradiation. Since the results of 20 bands division and 40 bands division match very well in perpendicular irradiation case, while the other three plots are relatively far from the two, we can assume 20 bands division to be the optimal choice at the moment. More comparison will be given in next chapter to check out whether the 20 bands division can best represent energy allocation in system under all incoming angle cases.

Fig 4.5 shows total energy harvest in water and louver, of different band numbers.

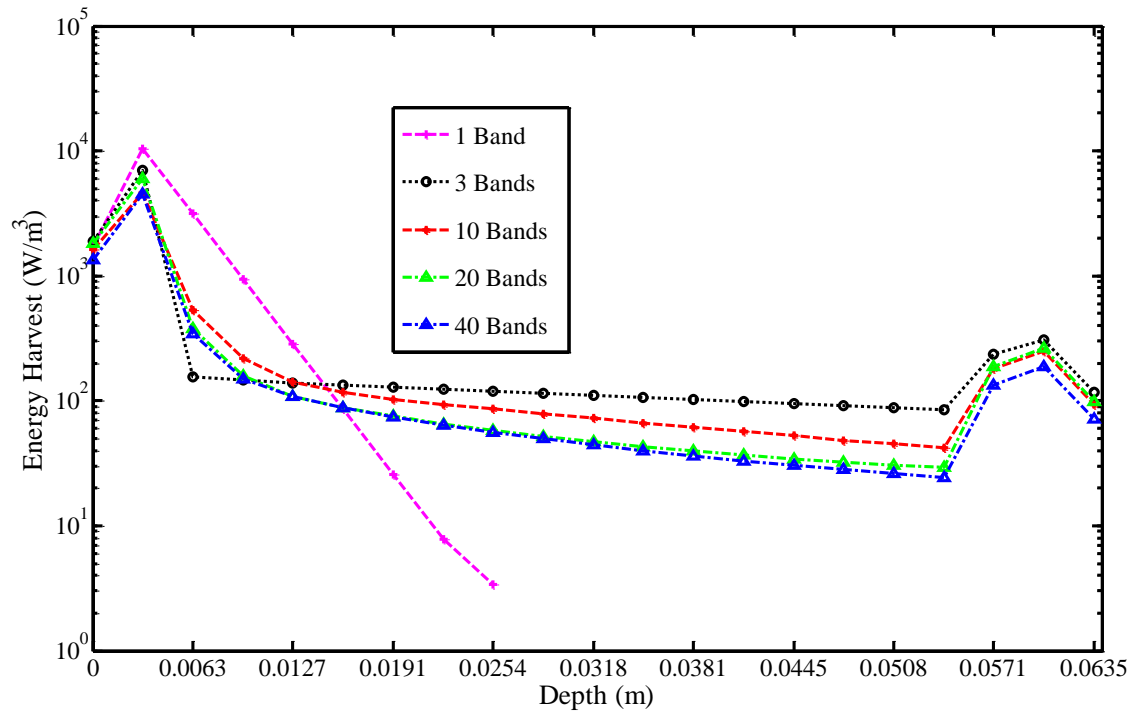


Fig 4.4 Centerline energy allocation of different bands

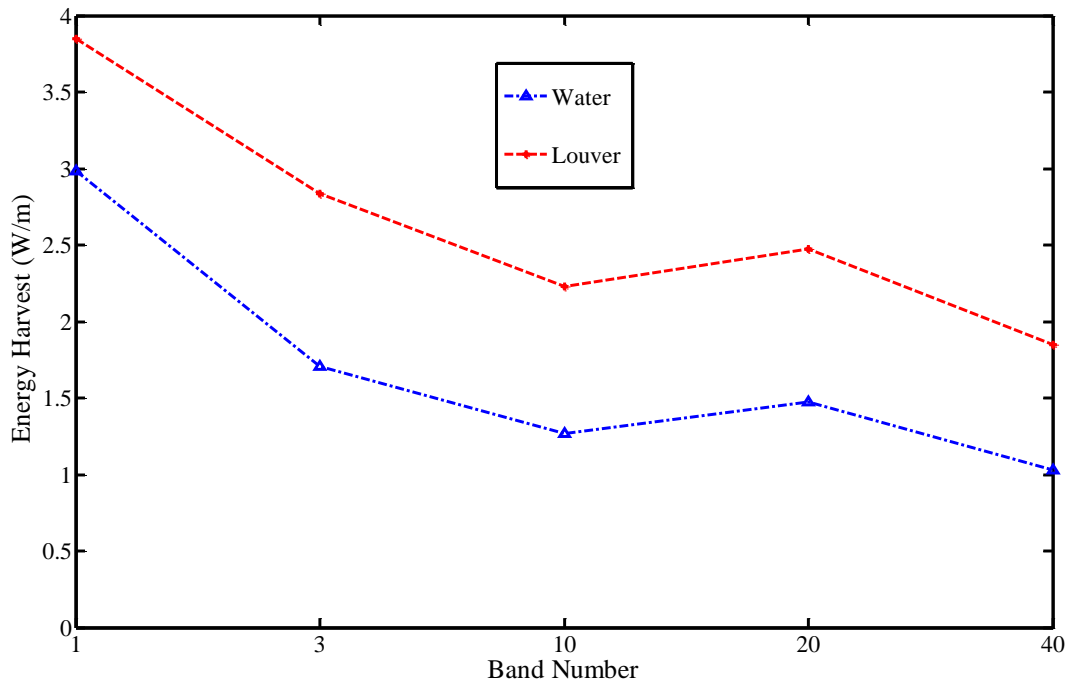


Fig 4.5 Total energy harvest in water and louver of different bands

The total energy harvest in water and louver varies with band number. The variation might be due to accumulative error during numerical calculation on bands with smaller water absorptivities. Smaller absorptivities mean more times an energy bundle is redirected before fully absorbed, thus leading to more overall accumulative error. The energy harvest of uniform band division is much higher than the rest since water absorptivity is inaccurately estimated at $O(2)$ over full spectrum. But if we kick out the largest value (1 band result) and the smallest value (40 bands result), the result of 20 bands is approximately the average value of the three results remained. This means choosing the division of 20 bands can guarantee the accuracy required.

Chapter 5

Influence of Incident Direction

5.1 Choice of Spectral Band Number

The incoming direction of solar irradiation onto a fixed surface on the ground varies due to the change in solar position at different times during the day. Accurate algorithm regarding solar position calculation can be found in ref.[104]. All results given in this thesis are considered under $\phi = \pi$ case for convenience. Fig 5.1 shows how ϕ angle is defined in this thesis.

Centerline energy allocation plots of three representative incident directions, $\theta = 0$, $\theta = \frac{\pi}{6}$, and $\theta = \frac{\pi}{3}$, are given below. Fig 4.4 has already appeared in chapter 4, but it's again listed below to make comparisons with the other two figures with different incoming angles. From Fig 4.4, Fig 5.2 and Fig 5.3, we can see that the results of 20 bands division and 40 bands division match best overall, which certifies the conclusion at the end of last

chapter that 20 bands division is the optimal choice under current simulation condition. In calculations that follow, 20 bands division will be used while changing other parameters.

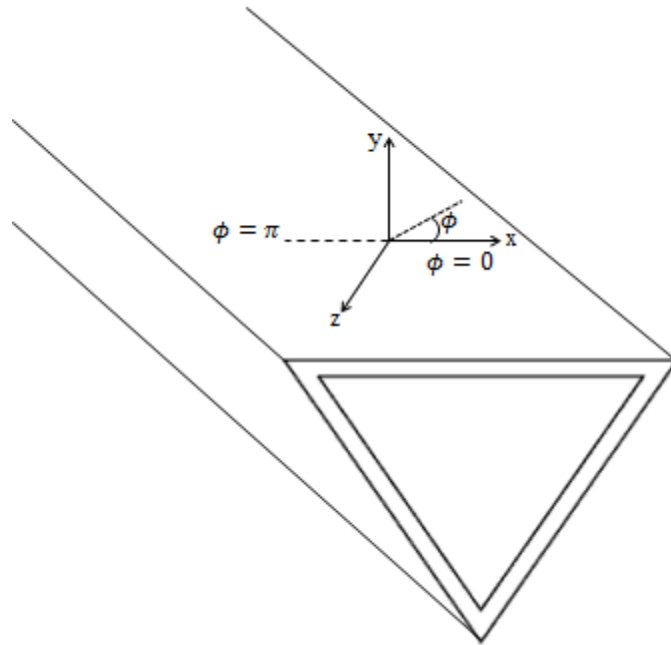
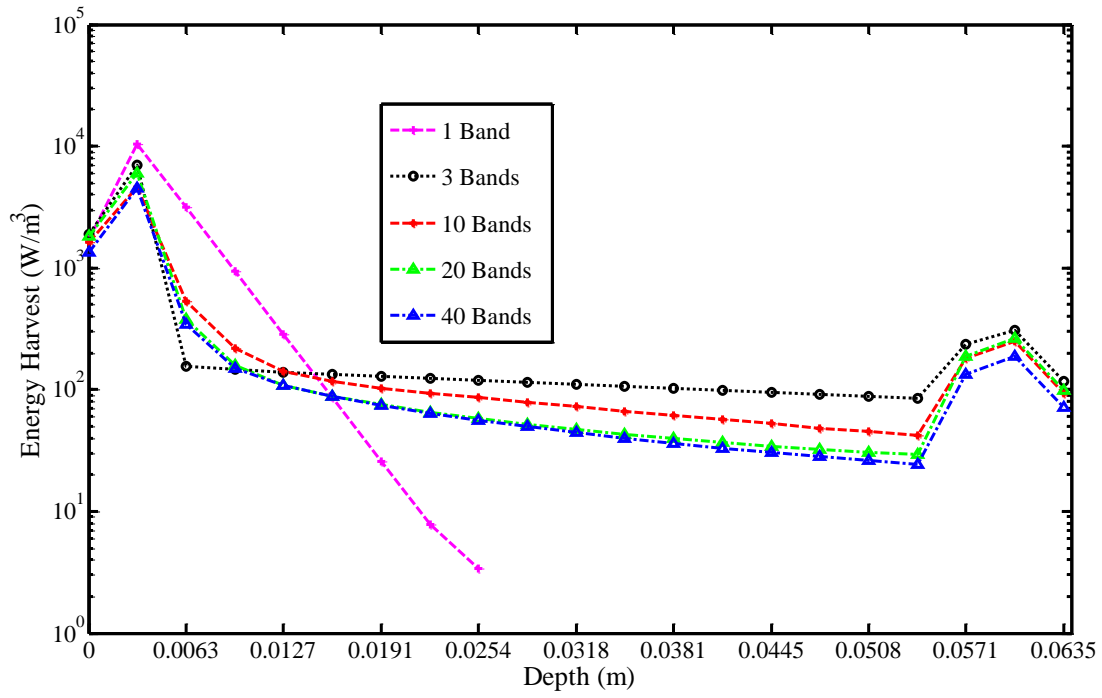
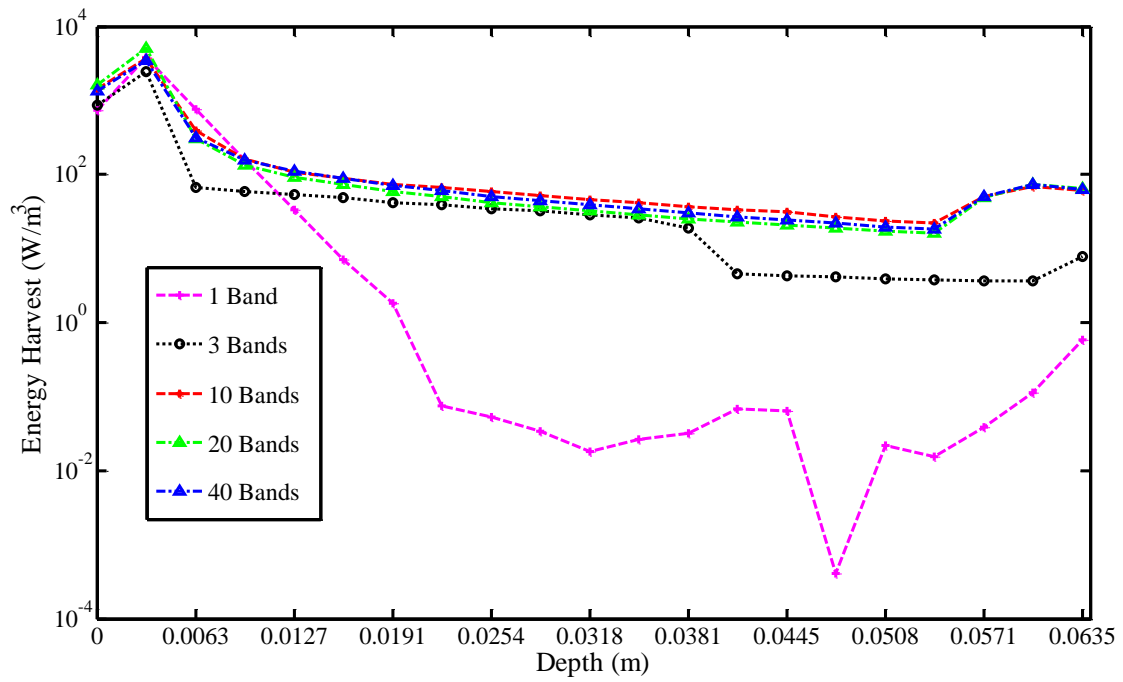


Fig 5.1 Illustration of $\phi = 0$ irradiation

Fig 4.4 $\theta = 0$ irradiationFig 5.2 $\theta = \frac{\pi}{6}$ irradiation

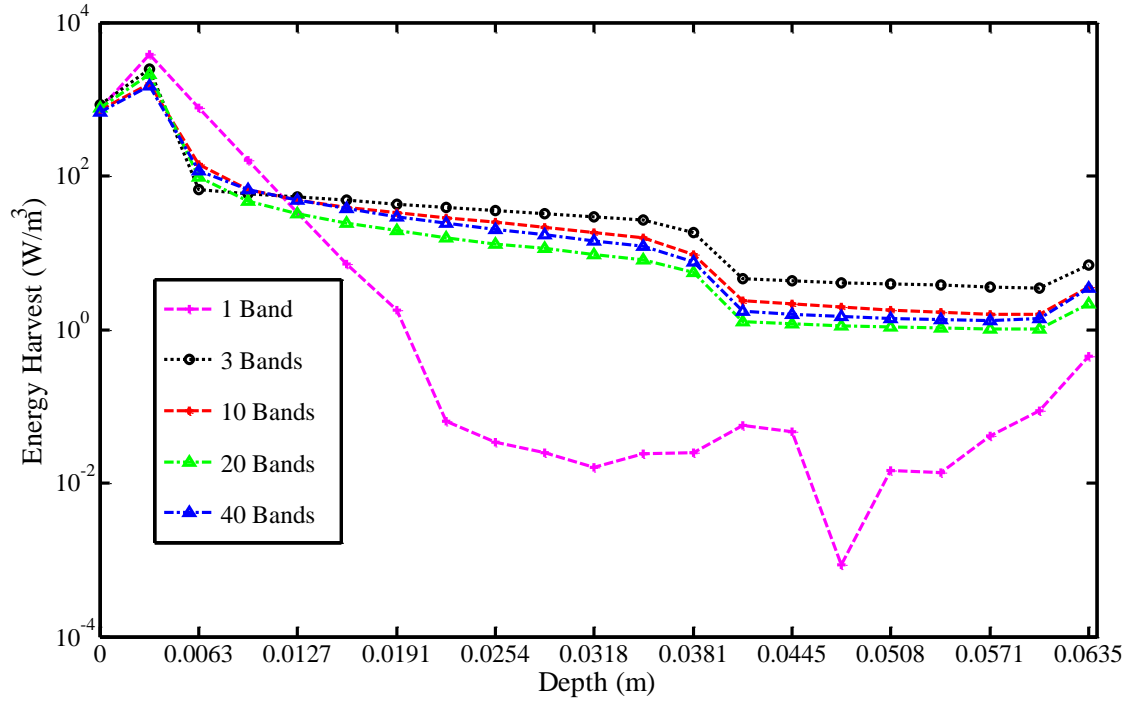


Fig 5.3 $\theta = \frac{\pi}{3}$ irradiation

5.2 Angular Variation Analysis

Fig 5.4 gives energy distribution along centerlines with various incoming angles. We can see that the orientation of system plays an important role in energy harvest. The obvious drops appears at incoming angle 60° in Fig 5.4 is due to the geometry of the system.

With incoming angle almost perpendicular to one boundary of system (incoming angle of 60° is exactly perpendicular to left hand side boundary illustrated in Fig. 5.1), a large portion of solar irradiation leaves the system almost perpendicularly through silica glass, traveling very short distance, without being redirected back into system. We can also see that at small incoming angles, energy harvest gradually differs as penetration depth grows. Energy harvest in grids close to surface facing irradiation are not obviously affected when incoming angles are relatively small, since under small incoming angles, energy bundles always pass through these grids before hit a surface. However, for grids deep

inside the louver, energy harvest is mostly realized through redirected energy bundles, which makes the energy harvest more dependent on incoming angles.

Irradiation with incoming angle 90° doesn't enter the system at all, thus in this case the total energy harvest is 0 everywhere in the system.

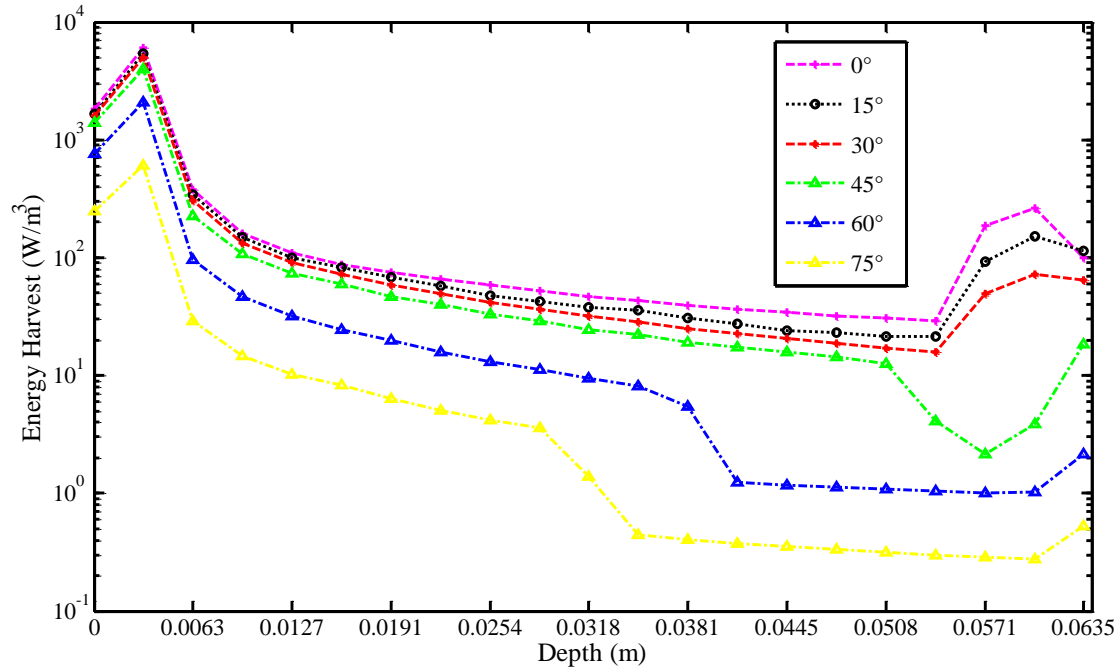


Fig 5.4 Angular variation of centerline energy distribution

Fig 5.5 shows total energy harvest in water of 20 bands division with incoming angles varying from 0° to 90° with step size 5° . The continuous dashed curve is created by curve fitting. The total energy harvest in Fig 5.5 first drops slowly. Then around 45° incoming angle, the falling down trend becomes relatively sharp, and the trend is again slowed down as incoming angle becomes close to 90° . This agrees with the observation from Fig 5.4 that there is an obvious drop in total energy harvest at around 45° incoming angle.

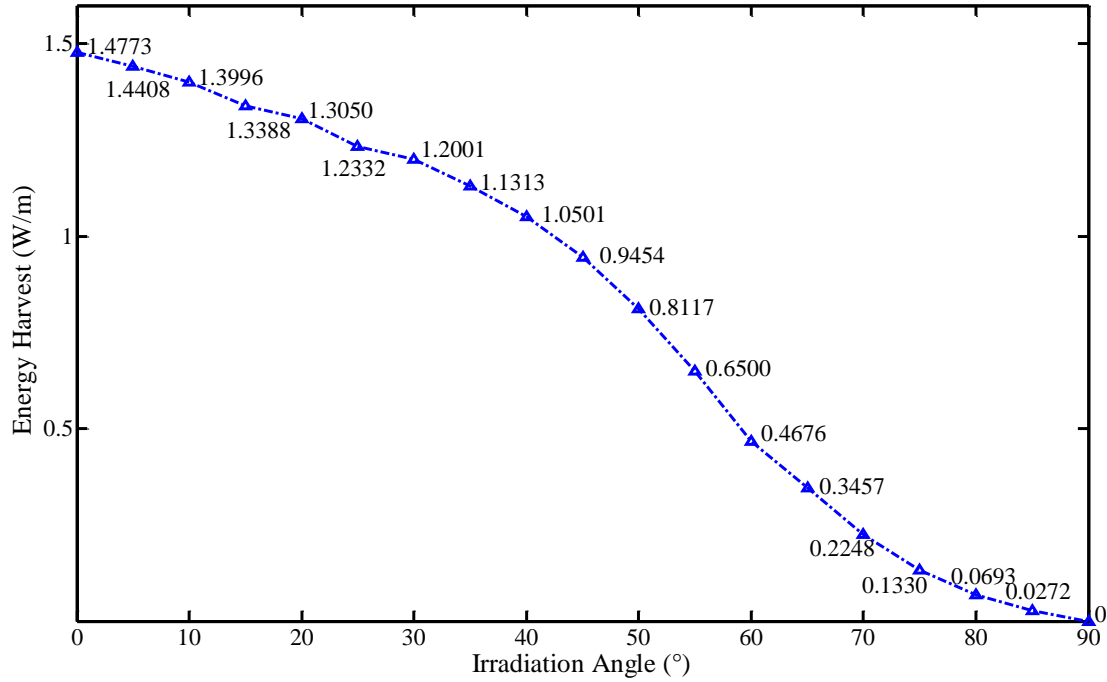


Fig 5.5 Angular variation of total energy harvest in water

5.3 Contour of Louver

The contours of $\theta = 0$, $\theta = \frac{\pi}{6}$, and $\theta = \frac{\pi}{3}$ irradiation are given in Fig 5.6, Fig 5.7 and Fig 5.8 below. We can see that in $\theta = \frac{\pi}{3}$ case, where incoming irradiation is perpendicular to left hand surface, energy harvest is obviously much less than that in the other two cases. Here we do not consider $\theta = \frac{\pi}{2}$ since in that case, irradiance doesn't enter the louver system and the energy accumulation in the system is 0.

In Fig 5.6, energy allocation is symmetric, and energy harvest is more concentrated in corners and grids closer to irradiated surface, where irradiation can be more easily trapped and its intensity has not yet been obviously attenuated. The highest energy harvest appears at left and right hand side corners, where irradiation is trapped in the

narrow corner between two interfaces and travels much longer distances before complete absorption is obtained.

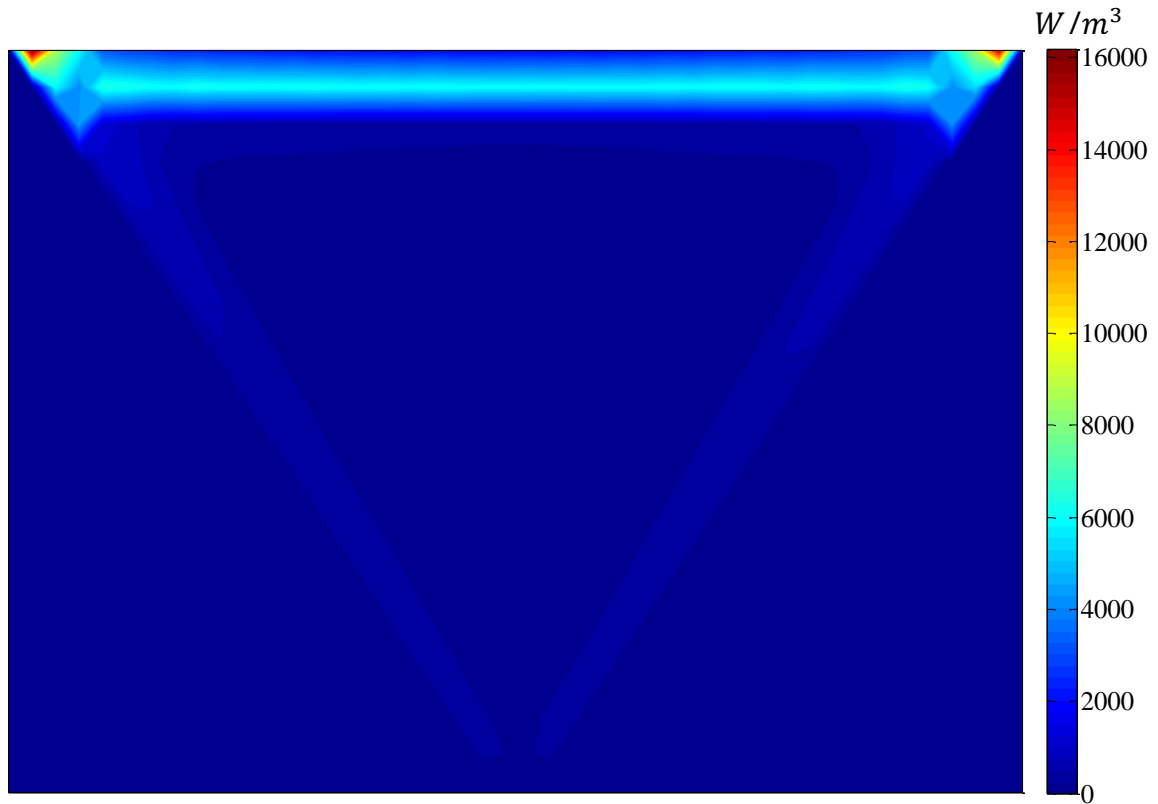


Fig 5.6 $\theta = 0$ irradiation contour

In FORTRAN program, in order to avoid dead end in corners while running program, a maximum reflection time of 1000 has been set. After 1000 redirections in one corner, the energy remained in a bundle is added to the last grid it passes through. This may seem inaccurate for one single energy bundle. But most corners consist of two grids at most, and each trapped energy bundle has to end up in one of the two corner grids. Since we are applying the Monte Carlo method based on a huge sample size (10^8 energy bundles), setting an upper limit for redirection in a corner is accurate. The symmetric contour in Fig 5.6 has certified the accuracy of this method.

The bright area around bottom part in Fig 5.7 is also because energy accumulates more easily in bottom corner. Top right hand side corner in Fig 5.7 accumulates more energy since the orientation of the irradiation surface makes energy bundles easily trapped in this corner.

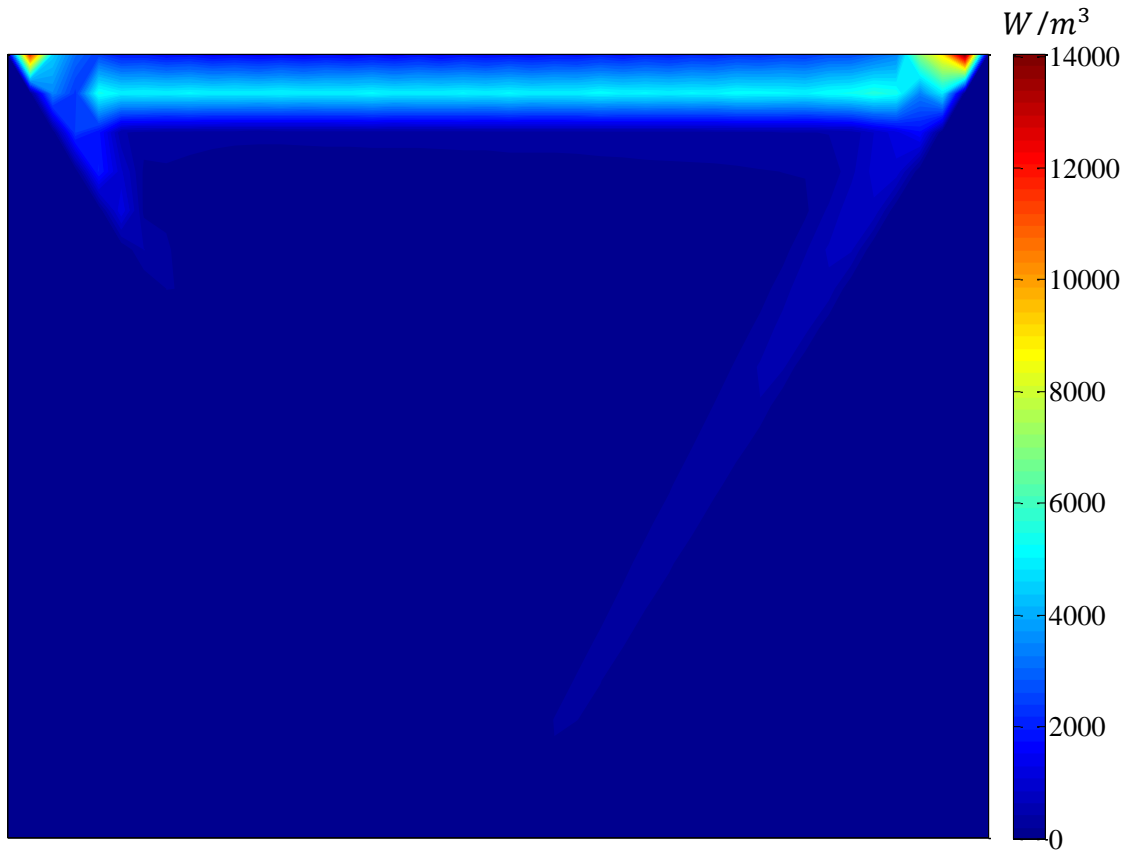


Fig 5.7 $\theta = \frac{\pi}{6}$ irradiation



Fig 5.8 $\theta = \frac{\pi}{3}$ irradiation

In Fig 5.8, the asymmetry is even more obvious and we can find there is hardly any energy harvest on left hand side boundary of the louver. This is because when irradiation angle becomes $\frac{\pi}{3}$, the redirected irradiation reaching right hand side boundary is almost perpendicular to the interface, thus most irradiation leave the louver directly without being redirected to the other boundaries.

Chapter 6

Conclusion

This thesis focuses on solar radiation simulation of a smart window aimed at harvesting collimated solar irradiation and providing better lighting by changing the penetration depth of sunlight into the room. The model of smart window is a series of silica glass louvers with water flowing inside as energy absorption and storage medium. The heat harvest of collimated solar irradiation inside a silica glass louver has been studied in this thesis. The triangular tubes are filled with water and solar irradiation comes into the system in arbitrary directions and is at full spectrum. Triangular meshes are used so that the interfaces are automatically placed on the edges of grids. Monte Carlo method is used to decide between diffuse reflection, total reflection and refraction on interface, and the direction of ray leaving interface after being redirected. Forward ray tracing method is used to allocate the energy harvest into individual grids along ray path. Besides, full solar spectrum has been divided into multiple bands, band averaged medium properties on each band are obtained, and energy harvest inside louver is simulated in FORTRAN.

Comparison of results from different band division methods and different energy bundle numbers has been made in order to find optimal parameters for numerical calculation.

There exists an optimal sample size for the Monte Carlo method. Either too small or too large sample sizes leads to inaccuracy. In the case being studied, $N_{RAY}=10^8$ is the optimal sample size which saves CPU time and guarantees accuracy requirements.

Band division is important for solar irradiation calculation. Due to various medium properties being used (water and glass properties in this thesis), the full solar spectrum should be divided into different discrete bands that are equivalent in energy to have similar weight. Also, medium property profiles should be relatively smooth on each band since we use integrated properties for each band. In the case studied in this thesis, a band number of 20 is the optimal band number.

Energy harvest differs a lot at different wavelengths. This indicates that we can truncate different wavelength ranges to make better use of solar irradiation.

Orientation of louver is important in energy harvest. The big difference of energy harvest at various incoming directions can be found in the last chapter. Since the orientation of the louver is fixed in the case studied, an optimal orientation needs to be found based on daily direction variation of solar irradiation. However, if diffuse irradiation is added to the calculation, more average behaviors should be expected with various incoming directions.

The efficiency of the smart window device still needs improvement. Instead of harvesting solar irradiation using a tinted surface, the smart window device studied in this thesis tries to harvest solar irradiation using a water volume. Considering only the radiation part,

energy harvest in water is obviously less than energy harvest in whole louver, which means that most of the heat is still in silica glass wall. Considering natural convection, the energy harvest in silica glass will soon dissipate into the environment leading to energy loss. More ways should be taken to make energy bundles travel longer distance in water, or to add certain paint on outer surface of silica glass to redirect the infrared solar irradiation back into louver, in order to get more efficient performance in the smart window.

Reference

- [1] Vaclav Smil, *Energy: A Beginner's Guide*, Oneworld Publications, 2006.
- [2] Matthew T. Lawder, Vilayanur Viswanathan, Venkat R. Subramanian, Balancing autonomy and utilization of solar power and battery storage for demand based microgrids, *Journal of Power Sources*, Vol. **279**, pp.645-655, 2015
- [3] A.G. Imenes, D.R. Mills, Spectral beam splitting technology for increased conversion efficiency in solar concentrating systems: a review, *Solar Energy Materials & Solar Cells*, Vol. **84**, pp.19-69, 2004.
- [4] Massimo Lazzaroni, Stefano Ferrari, Vincenzo Piuri, Ayse Salman, Loredana Cristaldi, Macro Faifer, Models for solar radiation prediction based on different measurement sites, *Measurement*, Vol. **63**, 2015, pp.346-363
- [5] John A. Duffie, William A. Beckman, *Solar Engineering of Thermal Processes*, 1980, John Wiley & Sons, p3
- [6] <http://www.science-story.com/scaled-solar-system-poster.php>
- [7] Smith E. V. P., Gottlieb D. M., Solar Flux and its Variations, *Space Science Reviews*, Vol. **16**, pp.771-802, 1974.
- [8] R. Shankar, *Principles of Quantum Mechanics*, Second edition, Springer, pp.197
- [9] J. Baker, M. Douma, S. Kotochigova, (available at: <http://physics.nist.gov>) *National Institute of Standards and Technology*, 2011
- [10] Michael F. Modest, Radiative Heat Transfer, Second edition, Academic Press, 2003.
- [11] John R. Howell, Robert Siegel, M. Pinar Mengüç, Thermal Radiation Heat Transfer, Fifth edition, CRC Press, 2011.
- [12] Adrain Bejan, *Convection Heat Transfer*, Third edition, John Wiley & Sons, Inc, 2004
- [13] Energy Information Administration, 2003 Commercial Buildings Energy Consumption Survey, Table E1.
- [14] Wiesenfarth M, Helmers H, Philipps SP, Steiner M, Bett AW, Advanced concepts in concentrating photovoltaics (CPV), 27th European Photovoltaic Solar Energy Conference and Exhibition, Frankfurt (Germany), 2012. pp. 11-15.

- [15] Martin A. Green, Keith Emery, Yoshihiro Hishikawa, Wilhelm Warta, Ewan D. Dunlop, Solar cell efficiency tables (Version 45), *Progress in Photovoltaics: Research and Applications*, Vol. **23**, Issue 1, 2014, pp.1-9.
- [16] <http://www.energygrant.com/brisbane-solar-resources/brisbane-solar-hot-water/>
- [17] http://upload.wikimedia.org/wikipedia/commons/6/66/Solar_panels_integrated_in_a_block_of_flats_in_Viikki_Helsinki_Finland.jpg
- [18] http://upload.wikimedia.org/wikipedia/commons/8/8f/Westmill_Solar_2.jpg
- [19] Mervin E. Muller, Review: J. M. Hammersley, D. C. Handscomb, Monte Carlo Methods; Yu. A. Shreider, Methods of Statistical Testing/Monte Carlo Method, *The Annals of Mathematical Statistics*, 1966, DOI: 10.1214, pp.532-538.
- [20] John R. Howell, Application of Monte Carlo to heat transfer problems, *Advances in Heat Transfer*, Vol. **5**, Academic Press, New York, 1968.
- [21] John R. Howell, The Monte Carlo Method in radiative Heat Transfer, 1997 Max Jacob Memorial Award Lecture, *Journal of Heat Transfer*, Vol. **120**, August 1998, pp.547-560.
- [22] L.N. Shchur, J.R. Heringa, H.W.J. Blöte, Simulation of a directed random-walk model, The effect of pseudo-random-number correlations, *Physica A*, Vol. **241**, 1997, pp. 579-592.
- [23] Karl Pearson, The problem of the random walk, *Nature*, Vol. **72**, 1905, pp. 294.
- [24] Gérard Le Caër, Two-step Dirichlet random walks, *Physica A*, Vol. **430**, 2015, pp. 201-215.
- [25] Gaston E. Barberis, Non-periodic pseudo-random numbers used in Monte Carlo calculations, *Physica B*, Vol. **398**, 2007, pp. 468-471.
- [26] Wen-jie Yang, Hiroshi Taniguchi, Kazuhiko kudo, Radiative Heat Transfer by the Monte Carlo Method, Academic Press, 1995.
- [27] <http://citeseerx.ist.psu.edu/viewdoc/download?doi=10.1.1.208.2177&rep=rep1&type=pdf>
- [28] David J. Kennison, Conpackt, A Contouring Package for Triangular Meshes, National Center for Atmospheric Research.
- [29] Eric A. Smith, Thomas H. Vonder Haar, John R. Hickey, Robert Maschhoff, The nature of the short period fluctuations in solar irradiance received by the earth, *Climate Change*, Vol. **5**, 1983, pp.211-235.
- [30] Thomas H. Vonder Haar, Verner E. Suomi, Measurements of the Earth's Radiation Budget from Satellites During a Five-Year Period. Part I: Extended Time and Space Means, *Journal of the Atmospheric Sciences*, Vol. **28(3)**, 1971, pp. 305-314.
- [31] Christian A. Gueymard, The sun's total and spectral irradiance for solar energy applications and solar radiation models, *Solar Energy*, Vol. **76**, 2004, pp. 423-453.
- [32] Solar constant and zero air mass solar spectral irradiance tables, Standard E490-00a, *The American Society for Testing and Materials*, 2000.
- [33] J. Glover, J. S. G. McCulloch, The empirical relation between solar radiation and hours of sunshine, *Quarterly Journal of the Royal Meteorological Society*, Vol. **84(360)**, 1958, pp. 172-175.
- [34] H. S. Cengiz, J. M. Gregory, J. L. Sebaugh, Solar Radiation Prediction from Other Climatic Variables, *TRANSACTIONS of the ASME*, Vol. **24**, 1981, pp. 1269-1272.

- [35] M.P. Thekaekara, Data on incident solar energy, *Supplement to the Proceedings of the 20th Annual Meeting of the Institute for Environmental Sciences*, Vol. **21**, 1974.
- [36] John H. Seinfeld, Spyros N. Pandis, *Atmospheric Chemistry and Physics: From Air Pollution to Climate Change*, 2nd Edition, Wiley, New York, 2006.
- [37] Alexandre Dal Pai, João F. Escobedo, Dinival Martins, Érico T. Teramoto, Analysis of hourly global, direct and diffuse solar radiations attenuation as a function of optical air mass, *Energy Procedia*, Vol. **57**, 2014, pp. 1060-1069.
- [38] World Meteorological Organization, *Manual on the global observing system*, Vol. **1**, 2003.
- [39] Alexander Kokhanovsky, Optical properties of terrestrial clouds, *Earth-Science Reviews*, Vol. **64**, 2004, pp.189-241.
- [40] John M. Wallace, Peter V. Hobbs, *Atmospheric Science: An Introductory Survey*, Academic Press, 2006.
- [41] P. Blanc, B. Espinar, N. Geuder, C. Gueymard, R. Meyer, R. Pitz-Paal, B. Reinhardt, D. Renné, M. Segupta, L. Wald, S. Wilbert, Direct normal irradiance related definitions and applications: The circumsolar issue, *Solar Energy*, Vol. **110**, 2014, pp. 561-577.
- [42] Fritz Kasten, Andrew T. Young, Revised optical air mass tables and approximation formula, *Applied Optics*, Vol. **28(22)**, 1989, pp. 4735-4738.
- [43] A.D. Watt, On the Nature and Distribution of Solar Radiation, *U.S. Department of Energy Report HCP/T2552-01*, 1978.
- [44] Constantinos P Jacovides, Michael D Steven, Demonsthenis N Asimakopoulos, Spectral Solar Irradiance and Some Optical Properties for Various Polluted Atmospheres, *Solar Energy*, Vol. **69(3)**, 2000, pp. 215-227.
- [45] R. J Charlson, J Langner, H Rodhe, C. B Leovy, S. G Warren, Perturbation of the northern hemispheric radiative balance by backscattering from antropogenic surface aerosols, *Tellus*, Vol. **4AB**, 1991, pp. 152-163.
- [46] Stephen E. Schwartz, The whitehouse effect-Shortwave radiative forcing of climate by anthropogenic aerosols : an overview, *Journal of Aerosol Science*, Vol. **27(3)**, 1996, pp. 359-382.
- [47] Standard Tables for Reference Solar Spectral Irradiances: Direct Normal and Hemispherical on 37° Tilted Surface, *ASTM Book of Standards*, Vol. **14(04)**, 2012.
- [48] Lord Rayleigh, On the electromagnetic theory of light, *Phil. Mag.*, Vol. **12**, 1881, pp. 81-101.
- [49] John William Strutt, Editorial Comment on the Science Papers of Lord Rayleigh, *Radio Science Journal of Research*, Vol. **69D(9)**, 1965, pp. 1307-1308.
- [50] Gustav Mie, Beiträge zur Optik trüber Medien, speziell kolloidaler Metallösungen, *Annalen der Physik*, vol. **330(3)**, 1908, pp. 377-445.
- [51] Barry A. Bodhaine, Norman B. Wood, Ellsworth G. Dutton, James R. Slusser, On Rayleigh Optical Depth Calculations, *Journal of Atmospheric and Oceanic Technology*, Vol. **16**, 1999, pp. 1854-1961.
- [52] Robert J. List, *Smithsonian meteorological tables*, Washington: Smithsonian Institution Press, 1968, pp. 527.
- [53] Christian Gueymard, SMARTS2, A Simple Model of the Atmospheric Radiative Transfer of Sunshine: Algorithms and performance assessment, 1995.

- [54] <http://oceancolor.gsfc.nasa.gov/WIKI/OCBandPass.html>
- [55] S. M. Anderson, J. Morton and K. Mauersberger, Near-infrared Absorption Spectra of $^{16}\text{O}_3$ and $^{18}\text{O}_3$: Adiabatic Energy of the $^1\text{A}_2$ State, *The Journal of Chemical Physics*, Vol. **93(6)**, 1990, pp. 3826-3832.
- [56] S. M. Anderson, J. Morton and K. Mauersberger, Effect of Isotopic Substitution on the Visible Absorption Spectrum of Ozone, *The Journal of Chemical Physics*, Vol. **94(10)**, 1991, pp. 6351-6357.
- [57] Stuart M. Anderson, Peter Hupalo and Konrad Mauersberger, Rotational Structure in the Near-infrared Absorption Spectrum of Ozone, *The Journal of Chemical Physics*, Vol. **99(1)**, 1993, pp. 737-739.
- [58] Stuart M. Anderson, Konrad Mauersberger, Laser Measurements of Ozone Absorption Cross Sections in the Chappuis Band, *Geophysical Research Letters*, Vol. **19(9)**, 1992, pp. 933-936.
- [59] Stuart M. Anderson, Peter Hupalo and Konrad Mauersberger, Ozone Absorption Cross Section Measurements in the Wulf Bands, *Geophysical Research Letters*, Vol. **20(15)**, 1993, pp. 1579-1582.
- [60] James B. Burkholder, Ranajit K. Talukdar, Temperature dependence of the ozone absorption spectrum over the wavelength range 410 to 760 nm, *Geophysical Research Letters*, Vol. **21(7)**, 1994, pp. 581-584.
- [61] R. L. McKenzie, W. A. Matthews and P. V. Johnston, The relationship between erythral UV and ozone, derived from spectral irradiance measurements, *Geophysical Research Letters*, Vol. **18(12)**, 1991, pp. 2269-2272.
- [62] Bogumil K., Orphal J., Homann T., Voigt S., Spietz P., Fleischmann O. C., Vogel A., Hartmann M., Kromminga H., Bovensmann H., Frerick J., Burrows J. P., Measurements of molecular absorption spectra with the SCIAMACHY pre-flight model: instrument characterization and reference data for atmospheric remote-sensing in the 230-2380 nm region, *Journal of photochemistry and photobiology A: Chemistry*, Vol. **157(2-3)**, 2003, pp. 167-184.
- [63] Wolfgang Schneider, Geert K. Moortgat, Geoffrey S. Tyndall, John P. Burrows, Absorption cross-sections of NO₂ in the UV and visible region (200 – 700 nm) at 298 K, *Journal of photochemistry and photobiology A: Chemistry*, Vol. **157(2-3)**, 1987, pp.195-217.
- [64] http://oceancolor.gsfc.nasa.gov/REPROCESSING/R2009/sources/k_no2.txt
- [65] Joseph H. Pierluissi and Chang-Ming Tsai, New LOWTRAN models for the uniformly mixed gases, *Applied Optics*, Vol. **26(4)**, 1987, pp. 616-618.
- [66] Joseph H. Pierluissi and Ken Tomiyama, Numerical methods for the generation of empirical and analytical transmittance functions with applications to atmospheric trace gases, *Applied Optics*, Vol. **19(14)**, 1980, pp. 2298-2309.
- [67] Joseph H. Pierluissi and Chang-Ming Tsai, Molecular transmittance band model for oxygen in the visible, *Applied Optics*, Vol. **25(15)**, 1986, pp. 2458-2460.
- [68] A. H. Maghrabi, H. M. Al Dajani, Time distribution of the precipitable water vapor in central Saudi Arabia and its relationship to solar activity, *Advances in Space Research*, Vol. **53(8)**, 2014, pp. 1169-1179.

- [69] Smithsonian Meteorological Tables, *Smithsonian Miscellaneous Collections*, 5th edition, 1984, pp. 350.
- [70] A. Weler and R. W. Hyland, Formulations for the Thermodynamic Properties of the Saturated Phases of H_2O from 173.15 to 473.15 K, and of Saturated Moist Air from 173.15 K to 372.15 K, at Pressures to 5 MPa, *ASHRAE Transactions*, Vol. **89(2)**, 1983, pp. 520-535.
- [71] Goff, J. A. Saturation pressure of water on the new Kelvin temperature scale, *Transactions of the American society of heating and ventilating engineers*, 1957, pp 347-354.
- [72] Buck, A. L., New equations for computing vapor pressure and enhancement factor, *Journal of Applied Meteorology*, Vol. **20**, 1981, pp. 1527-1532.
- [73] Murphy, D. M. and T. Koop, Review of the vapour pressures of ice and supercooled water for atmospheric applications, *Quarterly Journal of the Royal Meteorological Society*, Vol. **131(608)**, 2005, pp. 1539-1565.
- [74] M. Putsay, T. Tanczer, V. Vadász, Determination of precipitable water by using water-vapor image taken from MOS-1, *Advances in Space Research*, Vol. **12(7)**, 1992, pp. 229-232.
- [75] Raymond C. Smith and Karen S. Baker, Optical properties of the clearest natural waters (200–800 nm), *Applied Optics*, Vol. **20(2)**, 1981, pp. 177-184.
- [76] E. Montilla, S. Mogo, V. Cachorro, A. de Frutos, An integrating sphere spectral system to measure continuous spectra of aerosol absorption coefficient, *Journal of Aerosol Science*, Vol. **42(3)**, 2011, pp. 204-212.
- [77] A. A. Kokhanovsky and E. P. Zege, Optical Properties of Aerosol Particles: A Review of Approximate Analytical Solutions, *Journal of Aerosol Science*, Vol. **28(1)**, 1997, pp. 1-21.
- [78] H. Moosmüller, R.K. Chakrabarty, W.P. Arnott, Aerosol light absorption and its measurement: A review, *Journal of Quantitative Spectroscopy and Radiative Transfer*, Vol. **110(11)**, 2009, pp. 844-878.
- [79] <http://www.co2offsetresearch.org/aviation/RF.html>
- [80] V. Ramaswamy, O. Boucher, J. Haigh, D. Hauglustaine, J. Haywood, G. Myhre, T. Nakajima, G. Y. Shi, S. Solomon, Radiative Forcing of Climate Change (chapter 6), *Climate Change 2001: The Scientific Basis*, 2001.
- [81] Keith P Shine, Piers M. de F Foster, The effect of human activity on radiative forcing of climate change: a review of recent developments, *Global and Planetary Change*, Vol. **20(4)**, 1999, pp. 205-225.
- [82] Ilias M. Vardavas, Frederic W. Taylor, Radiation and climate: atmospheric energy budget from satellite remote sensing, *International Series of Monographs on Physics*, Oxford Science Publications, 2011.
- [83] A. Kokhanovsky, Optical properties of terrestrial clouds, *Earth-Science Reviews*, Vol. **64**, 2004, pp. 189-241.
- [84] R.A. Schiffer, W.B. Rossow, The International Satellite Cloud Climatology Project (ISCCP): The First Project of the World Climate Research Programme, *Bulletin of the American Meteorological Society*, Vol. **64(7)**, 1983, pp. 779-784.

- [85] S. Menon, V.K. Saxena, P. Durkee, B.N. Wenny, K. Nielsen, Role of sulfate aerosols in modifying the cloud albedo: a closure experiment, *Atmospheric Research*, Vol. **61(3)**, 2002, pp. 169-187.
- [86] William B. Rossow, Robert A. Schiffer, Advances in Understanding Clouds from ISCCP, *Bulletin of the American Meteorological Society*, Vol. **80(11)**, 1999, pp. 2261-2287.
- [87] Robert F. Cahalan, William Ridgway, Warren J. Wiscombe, Thomas L. Bell, The Albedo of Fractal Stratocumulus Clouds, *Journal of the Atmospheric Sciences*, Vol. **51(16)**, 1994, pp. 2434-2455.
- [88] R.F. Cahalan, L. Oreopoulos, G. Wen, A. Marshak, S.C. Tsay, T. DeFelice, Cloud characterization and clear-sky correction from Landsat-7, *Remote Sensing of Environment*, Vol. **78(1-2)**, 2011, pp.83-98.
- [89] K. S. Shifrin, Scattering of Light in a Turbid Medium, (NASA Technical Translation TT F-477), 1968.
- [90] Marilyn F. Bishop, Calculations of Scattered Light from Rigid Polymers by Shifrin and Rayleigh-Debye approximations, *Biophysical Journal*, Vol. **56(5)**, 1989, pp. 911-925.
- [91] Benjamin Y. Liu, Richard C. Jordan, The Interrelationship and Characteristic Distribution of Direct, Diffuse and Total Solar Radiation, *Solar Energy*, Vol. **4(3)**, 1960, pp.1-19.
- [92] Achim Woyte, Ronnie Belmans, Johan Nijs, Fluctuations in instantaneous clearness index: Analysis and statistics, *Solar Energy*, Vol. **81**, 2007, pp. 195-206.
- [93] D. A. Ronzio, E. Collino, P. Bonelli, A survey on different radiative and cloud schemes for the solar radiation modeling, *Solar Energy*, Vol. **98**, 2013, pp. 153-166.
- [94] H. Suehrcke, P.G. McCormick, The diffuse fraction of instantaneous solar radiation, *Solar Energy*, Vol. **40(5)**, 1988, pp. 423-430.
- [95] Marco Bindi, Francesco Miglietta, Gaetano Zipoli, Different methods for separating diffuse and direct components of solar radiation and their application in crop growth models, *Climate Research*, Vol. **2**, pp. 47-54, 1992.
- [96] L. T. Wong, W. K. Chow, Solar radiation model, *Applied Energy*, Vol. **69**, pp. 191-224, 2001.
- [97] Christian A. Gueymard, The suns total and spectral irradiance for solar energy applications and solar radiation models, *Solar Energy*, Vol. **76**, 2003, pp. 423-453.
- [98] United States Committee on Extension to the Standard Atmosphere, "U.S. Standard Atmosphere, 1976", National Oceanic and Atmospheric Administration, National Aeronautics and Space Administration, United States Air Force, Washington D.C., 1976.
- [99] Maatouk Khoukhi, Shigenao Maruyama, Stephen Bosi and Atsuki Komiya, A Simple Approach for Calculating the Optical Constants of a Clear Glass Window From 0.19 to 5 μm , *Recent Developments in Solar Energy*, Nova Publishers, 2007.
- [100] M. Herzberger, The Dispersion of Optical Glass, *Journal of the Optical Society of America*, Vol. **32(2)**, 1942, pp. 70-72.
- [101] M. Rubin, Optical properties of soda lime silica glasses, *Solar Energy Materials*, Vol. **12(4)**, 1985, pp. 275-288.
- [102] G. M. Hale and M. R. Querry. Optical Constants of Water in the 200-nm to 200- μm Wavelength Region, *Applied Optics*, Vol. **12(3)**, 1973, pp. 555-563.

- [103] John M. Jarem, Joseph H. Pierluissi, and Michael Maragoudakis, Numerical methods of band modeling and their application to atmospheric nitrous oxide, *Applied Optics*, Vol. **23(3)**, 1984, pp.406-410.
- [104] Joseph J. Michalsky, The Astronomical Almanac's algorithm for approximate solar position (1950-2050), *Solar Energy*, Vol. **40(3)**, 1988, pp. 227-235.